



Flight Investigation of the Effects of Pressure-Belt Tubing Size on Measured Pressure Distributions

Natale A. Rivers

Langley Research Center, Hampton, Virginia

Cornelious P. van Dam

University of California at Davis, Davis, California

Phillip W. Brown

Langley Research Center, Hampton, Virginia

Robert A. Rivers

Langley Research Center, Hampton, Virginia

The NASA STI Program Office . . . in Profile

Since its founding, NASA has been dedicated to the advancement of aeronautics and space science. The NASA Scientific and Technical Information (STI) Program Office plays a key part in helping NASA maintain this important role.

The NASA STI Program Office is operated by Langley Research Center, the lead center for NASA's scientific and technical information. The NASA STI Program Office provides access to the NASA STI Database, the largest collection of aeronautical and space science STI in the world. The Program Office is also NASA's institutional mechanism for disseminating the results of its research and development activities. These results are published by NASA in the NASA STI Report Series, which includes the following report types:

- **TECHNICAL PUBLICATION.** Reports of completed research or a major significant phase of research that present the results of NASA programs and include extensive data or theoretical analysis. Includes compilations of significant scientific and technical data and information deemed to be of continuing reference value. NASA counterpart of peer-reviewed formal professional papers, but having less stringent limitations on manuscript length and extent of graphic presentations.
- **TECHNICAL MEMORANDUM.** Scientific and technical findings that are preliminary or of specialized interest, e.g., quick release reports, working papers, and bibliographies that contain minimal annotation. Does not contain extensive analysis.
- **CONTRACTOR REPORT.** Scientific and technical findings by NASA-sponsored contractors and grantees.
- **CONFERENCE PUBLICATION.** Collected papers from scientific and technical conferences, symposia, seminars, or other meetings sponsored or co-sponsored by NASA.
- **SPECIAL PUBLICATION.** Scientific, technical, or historical information from NASA programs, projects, and missions, often concerned with subjects having substantial public interest.
- **TECHNICAL TRANSLATION.** English-language translations of foreign scientific and technical material pertinent to NASA's mission.

Specialized services that complement the STI Program Office's diverse offerings include creating custom thesauri, building customized databases, organizing and publishing research results . . . even providing videos.

For more information about the NASA STI Program Office, see the following:

- Access the NASA STI Program Home Page at <http://www.sti.nasa.gov>
- Email your question via the Internet to help@sti.nasa.gov
- Fax your question to the NASA STI Help Desk at (301) 621-0134
- Telephone the NASA STI Help Desk at (301) 621-0390
- Write to:
NASA STI Help Desk
NASA Center for AeroSpace Information
7121 Standard Drive
Hanover, MD 21076-1320

NASA/TM-2001-209857



Flight Investigation of the Effects of Pressure-Belt Tubing Size on Measured Pressure Distributions

Natale A. Rivers

Langley Research Center, Hampton, Virginia

Cornelious P. van Dam

University of California at Davis, Davis, California

Phillip W. Brown

Langley Research Center, Hampton, Virginia

Robert A. Rivers

Langley Research Center, Hampton, Virginia

National Aeronautics and
Space Administration

Langley Research Center
Hampton, Virginia 23681-2199

November 2001

Available from:

NASA Center for AeroSpace Information (CASI)
7121 Standard Drive
Hanover, MD 21076-1320
(301) 621-0390

National Technical Information Service (NTIS)
5285 Port Royal Road
Springfield, VA 22161-2171
(703) 605-6000

Contents

List of Tables	iv
List of Figures	iv
Symbols	vii
Summary	1
Introduction	1
Experimental Setup and Test Procedures	2
Instrumentation	2
Flight Test Procedure	6
Computational Method	6
Results	7
Flight Test	7
Computational Analysis	7
Discussion	9
Conclusions	10
Appendix A—Research Airplane	12
Appendix B—Flow Stagnation Sensor	15
Appendix C—Methodology for Obtaining Accurate Airfoil Coordinates	20
Appendix D—Airspeed Calibration Methodology	21
Appendix E—Flow-Direction and Velocity Sensor	23
References	25

List of Tables

Table 1.	Pressure-Belt Physical Characteristics and Configuration	2
Table 2.	Pressure Port Locations.....	4
Table 3.	Summary of Measurements List.....	6
Table 4.	Test-Point Summary.....	8
Table A1.	Airplane Physical Characteristics	13
Table B1.	Pressure Port Locations and Corresponding FSS Elements.....	15

List of Figures

Figure 1.	Wing instrumentation and belt configuration	26
Figure 2.	Wing modification	26
Figure 3.	Pressure belt arrangement on lower wing surface	26
Figure 4.	Needle modification.....	27
Figure 5.	ESP transducer	27
Figure 6.	Flow stagnation sensor	27
Figure 7.	Steady level flight test points	28
Figure 8.	Flight pressure distribution data for $C_L = 0.518$ and $M_\infty = 0.16$	28
Figure 9.	Flight pressure distribution data for $C_L = 0.824$ and $M_\infty = 0.13$	29
Figure 10.	Flight pressure distribution data for $C_L = 1.131$ and $M_\infty = 0.11$	29
Figure 11.	Computed pressure distribution data for $C_L = 0.518$, α (2D) = 3.3° , $M_\infty = 0.16$, and $R_c = 4.8 \times 10^6$	30
Figure 12.	Computed pressure distribution data for $C_L = 0.824$, α (2D) = 6.6° , $M_\infty = 0.13$, and $R_c = 3.75 \times 10^6$	30
Figure 13.	Computed pressure distribution data for $C_L = 1.131$, α (2D) = 9.0° , $M_\infty = 0.11$, and $R_c = 3.22 \times 10^6$	31
Figure 14.	Computed pressure distribution data for OD = 0.0625 in., $C_L = 0.824$, α (2D) = 6.0° , $M_\infty = 0.13$, and $R_c = 3.75 \times 10^6$	31
Figure 15.	Computed pressure distribution data for OD = 0.1250 in., $C_L = 0.824$, α (2D) = 6.6° , $M_\infty = 0.13$, and $R_c = 3.75 \times 10^6$	32
Figure 16.	Computed pressure distribution data for OD = 0.1875 in., $C_L = 0.824$, α (2D) = 6.6° , $M_\infty = 0.13$, and $R_c = 3.75 \times 10^6$	32
Figure 17.	Computed pressure distribution data for $C_L = 0.518$, α (2D) = 3.3° , $M_\infty = 0.16$, and $R_c = 4.8 \times 10^6$	33
Figure 18.	Computed and flight pressure distribution data for OD = 0.0625 in., $C_L = 0.519$, $M_\infty = 0.16$, and $R_c = 4.8 \times 10^6$	33

Figure 19. Computed and flight pressure distribution data for $OD = 0.1250$ in., $C_L = 0.519$, $M_\infty = 0.16$, and $R_c = 4.95 \times 10^6$	34
Figure 20. Computed and flight pressure distribution data for $OD = 0.1875$ in., $C_L = 0.519$, $M_\infty = 0.16$, and $R_c = 4.5 \times 10^6$	34
Figure 21. Computed and flight pressure distribution data for $OD = 0.0625$ in., $C_L = 0.825$, $M_\infty = 0.13$, and $R_c = 3.75 \times 10^6$	35
Figure 22. Computed and flight pressure distribution data for $OD = 0.1250$ in., $C_L = 0.824$, $M_\infty = 0.13$, and $R_c = 3.9 \times 10^6$	35
Figure 23. Computed and flight pressure distribution data for $OD = 0.1875$ in., $C_L = 0.824$, $M_\infty = 0.13$, and $R_c = 3.9 \times 10^6$	36
Figure 24. Computed and flight pressure distribution data for $OD = 0.0625$ in., $C_L = 1.131$, $M_\infty = 0.11$, and $R_c = 3.22 \times 10^6$	36
Figure 25. Computed and flight pressure distribution data for $OD = 0.1250$ in., $C_L = 1.131$, $M_\infty = 0.11$, and $R_c = 3.7 \times 10^6$	37
Figure 26. Computed and flight pressure distribution data for $OD = 0.1875$ in., $C_L = 1.131$, $M_\infty = 0.11$, and $R_c = 3.1 \times 10^6$	37
Figure A1. Research airplane	12
Figure B1. Flow stagnation and velocity sensor.....	16
Figure B2. Schematic of flow stagnation and velocity sensor	16
Figure B3. Measured pressure distribution data for $C_L = 0.36$, $M_\infty = 0.19$, $h = 6400$ ft, and $\alpha = 1.5^\circ$	17
Figure B4. Measured pressure distribution and FSS data for $h = 6400$ ft, $M_\infty = 0.12$, $\alpha = 6.3^\circ$, and $C_L = 0.84$	18
Figure B5. Pressure distribution and FSS data for $h = 6400$ ft, $M_\infty = 0.10$, $\alpha = 8.6^\circ$, and $C_L = 1.15$	19
Figure C1. Wing contour template.....	20
Figure D1. Curve fit of angle of attack versus pitch	22
Figure E1. Flow direction and velocity sensor	24
Figure E2. Flow direction and velocity sensor schematic.....	24

Symbols

a	speed of sound, knots
c	wing chord, ft
C_L	lift coefficient, $\frac{\text{Lift}}{q_\infty S}$
C_p	pressure coefficient, $\frac{p_1 - p_\infty}{q_\infty}$
$C_{p,\min}$	minimum pressure coefficient
$C_{p,s}$	pressure coefficient at stagnation
$C_{p,te}$	pressure coefficient at trailing edge
h	altitude, ft
M_∞	free-stream Mach number
p_c	free-stream static pressure calibrated, psf
Δp	position error, psf
p_l	local static pressure, psf
p_∞	free-stream static pressure, psf
q_c	dynamic pressure corrected, psf
q_∞	free-stream dynamic pressure, $\frac{\rho V^2}{2}$, psf
R_c	chord Reynolds number, $\frac{V_{Lc}}{n}$
S	reference wing area, ft ²
U_∞	free-stream velocity, knots
V	true airspeed, knots
V_{Lc}	calibrated airspeed, left, knots

W	aircraft weight, lb
x	chord location measured from leading edge
α	angle of attack, deg
α_L	angle of attack, left, deg
α_{Lc}	angle of attack corrected, $\frac{\alpha_L}{1.25}$, deg

ρ	density, slugs/ft ³
ν	kinematic viscosity, ft ² /sec

Abbreviations:

CTA	constant temperature anemometer
DC	direct current
ESP	electronically scanned pressure transducer
FSS	flow stagnation sensor
ISES	Inviscid Streamtube Euler Solver
LS	lower surface
MSES	Multielement Streamtube Euler Solver
NACA	National Advisory Committee for Aeronautics
OD	outer diameter, in.
PCM	pulse code modulated
TE	trailing edge
US	upper surface
WFF	Wallops Flight Facility
2D	two-dimensional

Summary

The pressure-belt technique is commonly used to measure pressure distributions on lifting and nonlifting surfaces where flush, through-the-surface measurements are not possible. The belts, made from strips of small-bore, flexible plastic tubing, are surface-mounted by a simple, nondestructive method. Additionally, the belts require minimal installation time, thus making them much less costly to install than flush-mounted pressure ports. Although pressure belts have been used in flight research since the early 1950s, only recently have manufacturers begun to produce thinner, more flexible tubing, and thin, strong adhesive tapes that minimize the installation-induced errors on the measurement of surface pressures. The objective of this investigation was to determine the effects of pressure-belt tubing size on the measurement of pressure distributions. For that purpose, two pressure belts were mounted on the right wing of a single-engine, propeller-driven research airplane. A flow stagnation sensor also was mounted on the leading edge of the right wing primarily to evaluate the sensor's in-flight reliability; its data also were used to verify the location of the stagnation point. All wing instrumentation was confined to a constant-chord ($c = 63.0$ in.) region of the wing located inboard of the aileron and outboard of the root region, and immersed in the propeller slipstream. The outboard pressure belt, consisting of 80 tubes, served as a baseline for the measurement and the comparison of effects. Each tube had an outer diameter (OD) of 0.0625 in. The inboard belt was used to evaluate three different tube sizes: 0.0625-, 0.1250-, and 0.1875-in. OD. The flight investigation for the unswept-belt configuration consisted of 13 data flights, including an airspeed calibration. Straight-and-level test points were conducted at pressure altitudes of 4500, 5500, 6500, and 8500 ft and indicated airspeeds ranging from 62 to 126 knots. The chord Reynolds number and free-stream Mach number ranged from 3.5×10^6 to 7.0×10^6 and 0.085 to 0.228, respectively.

A computational investigation of tube size on pressure distribution also was conducted using the two-dimensional Multielement Streamtube Euler

Solver (MSES) code. The true airfoil coordinates, as measured from the constant-chord section of the right wing, were modified in the MSES input files to account for the belt and the installation material (adhesive tape). The computed surface-pressure distributions are compared with the flight-pressure distributions at selected flight conditions for the three tube sizes.

Introduction

Accurate measurement of the surface pressure is a critical element of many flight research investigations. The preferred method of measuring surface pressures is the use of flush-mounted pressure taps. While flush ports offer an accurate means for measuring pressure distributions, they are not always practical. First, installation of flush-mounted pressure taps requires drilling holes through the skin, thus permanently marring the surface and often diminishing the structural integrity of the aircraft surface. Second, the installation of flush-mounted pressure taps may not be possible for either a wet wing or a wing with an internal fuel bladder. The requirement to make nonintrusive pressure measurements in a flight environment, with the accompanying large accelerations and high amplitude vibrations, led to development of the pressure-belt technique. The pressure belt provides a simple, nondestructive and economical means for measuring pressure distributions on wing surfaces and other bodies.

A pressure belt is a molded array of thin, small-bore, flexible, parallel plastic tubes whose outer diameters are tangent to one another. One end of each tube is sealed and the other end is connected to a pressure-measuring device. Each tube contains only a single orifice to measure local static pressure. In the present application, each orifice is located at a specified chordwise location. It is possible to map the chordwise pressure distribution about a spanwise location on the wing surface with the use of multiple tubes and by varying the chord location of each orifice (static port).

While pressure belts offer an inexpensive alternative to flush pressure orifices, they also have drawbacks. Mounting pressure tubing over

surface protrusions, such as round-head rivets and lap joints, can exaggerate surface roughness and waviness. As in the case with plumbing flush-mounted pressure orifices, routing the plastic tubing to the pressure scanners can be difficult, particularly when using pressure belts on multi-element wings.

Although pressure belts initially were used during the early 1950s for subsonic flight investigations, better materials, in the form of thinner, more flexible tubing and better adhesives, have improved installation methods and made possible the belts' use in both the transonic and supersonic flight regimes. In the past, pressure belts were installed using methods that locally raised the wing surface as much as 0.25 in. (ref. 1). Recently, installation methods and tubing sizes have reduced the additional surface thickness to as little as 0.067 in. Double-sided adhesive tape as thin as 0.005 in. can be used for mounting the tubing for subsonic flight testing (ref. 2). The focus of the research described in this report was to examine the effects of such improvements in the tube size and installation techniques on the measured wing pressure distributions.

A flight investigation was conducted at the NASA Langley Research Center. The right wing of a single-engine, general-aviation aircraft (appendix A) was instrumented with two pressure belts. The belt configuration is shown in figure 1. The tube outer diameter (OD) for the belts flown ranged from 0.0625 to 0.1875 in. In this report, tubing size is given as the tube outer diameter unless otherwise stated. Finally, this report also includes a comparison of measured stagnation location as determined by the flow stagnation sensor and the pressure belts.

Experimental Setup and Test Procedures

Instrumentation

The right wing of the research airplane was instrumented with two pressure belts and a flow stagnation sensor as shown in figure 1. All wing instrumentation was located on the

constant-chord section ($c = 63$ in.) outboard of the propeller slipstream. The outboard pressure belt remained unchanged throughout the entire flight test program and served as the baseline for pressure measurement comparisons. The tube size of the inboard pressure belt was systematically changed throughout the flight test program. Table 1 summarizes the flight-test instrumentation configurations: tube sizes, belt widths, number of active and inactive tubes, and inner and outer tube diameter. An important factor in determining the number of pressure ports that could be used was the spanwise length of the constant-chord section. Depending on the outer diameter of the tubing, it was possible to accommodate as many as 60 tubes and as few as 30 tubes on the inboard belt. In every case, three pressure transducers capable of monitoring 32 tubes each were used.

To provide a full chordwise pressure distribution as a baseline and to allow for a smooth continuous surface beneath the pressure belts, the

Table 1. Pressure-Belt Physical Characteristics and Configuration

Characteristic	Inboard	Outboard
Flights 1 and 2 (baseline):		
Belt width, in.	4.125	5.5
Number of tubes.....	60	80
Number of active tubes.....	0	78
Tube inner diameter, in.	0.028	0.028
Tube outer diameter, in.	0.0625	0.0625
Flights 3–7:		
Belt width, in.	4.125	5.5
Number of tubes.....	60	80
Number of active tubes.....	54	21
Tube inner diameter, in.	0.028	0.028
Tube outer diameter, in.	0.0625	0.0625
Flights 8–10:		
Belt width, in.	7.5	5.5
Number of tubes.....	60	80
Number of active tubes.....	54	21
Tube inner diameter, in.	0.046	0.028
Tube outer diameter, in.	0.1250	0.0625
Flights 11 and 12:		
Belt width, in.	5.8125	5.5
Number of tubes.....	30	80
Number of active tubes.....	28	19
Tube inner diameter, in.	0.096	0.028
Tube outer diameter, in.	0.1875	0.0625

gap between the wing and the wing flap was filled with a quick-drying rigid foam, smoothed flush with the wing surface, and covered with a strip of aluminum tape (fig. 2). Prior to installation of the pressure belt, the wing and the tubes were cleaned with a solvent to remove any grease or dirt from the wing surfaces. Next, the tubes, which came in strips of 10, were mounted on the wing surface with double-sided adhesive tape, 0.005 in. thick for the small and mid-size tubing, and 0.045 in. thick for the large tubing.

The outboard belt covered the entire chordwise surface from the trailing edge on the upper surface around the leading edge to the trailing edge on the lower surface. The inboard belt extended to only 20-percent chord on the lower surface before entering the wing through an access panel (fig. 3). Ideally, the tubing would extend across the full chord on both the upper and lower surface preventing surface discontinuities that might cause disturbances in the pressure distribution and disrupt the boundary layer. Once the tubing was mounted on the wing surface, the ends at the wing trailing edge were sealed with a quick-drying epoxy. The belts were then faired on each side with a smooth rubber epoxy. Next, a pressure tap was drilled into each tube at a specific chordwise location using a modified hypodermic needle of 0.003-in. OD. Figure 4 illustrates the modification to the needle that was made by beveling the outer edge 45° inward to produce a clean cut. Each hole was inspected with a microscope for burrs and other anomalies. If the quality of the hole was not satisfactory, it would be sealed and a new hole drilled upstream, relative to the pressure transducer, and in close proximity of the damaged hole.

Pressure port locations for each tube size are listed in table 2. After drilling the pressure ports, the tubes were then spliced to the internal tubes at the access panel. The internal tubes passed through the wing and into the fuselage. Inside the fuselage, each tube was connected to one of the three electronically scanned pressure (ESP) transducers (fig. 5).

Upon completion of the installation, the tubes were checked for leaks. This procedure required switching the internal calibration valve of each ESP transducer to the calibrate mode, applying a known pressure to each pressure port, and monitoring the electrical output of the ESP transducer for 30 sec to confirm that the tube could maintain the applied pressure. When the check was completed, the area at which the tubes were spliced was covered and aerodynamically smoothed with a rubber epoxy.

Pneumatic lag can pose a problem when trying to interpret the output of the pressure transducers connected to the pressure belts (ref. 3). The lag time for the longest tube (14 ft) with the smallest inner diameter (0.028 in.) was calculated to be less than 0.5 sec. A sufficiently long data acquisition time period and sufficiently high sample rate minimized the effects of pressure lag.

Three ESP transducers and signal-conditioning units for the pressure belts and flow stagnation sensor were housed on the instrumentation pallet located in the aft passenger compartment of the airplane. Table 3 lists the parameters measured in flight as well as several derived parameters. Most data were sampled at a rate of 6 Hz. Inside each ESP transducer unit is housed 32 individual pressure transducers. Each tiny transducer can provide an accurate pressure measurement by comparing the measured pressure at the pressure-belt port with a reference pressure. The information from the pressure transducers was then processed by a remote multiplexer/demultiplexer unit.

In addition to the pressure belts, a 2- by 2-in. flow stagnation sensor (FSS) (fig. 6) was mounted on the leading-edge surface inboard of the two pressure belts (fig. 1). The 60-element hot film sensor was able to indicate the location of the stagnation point with a 0.1-in. resolution, providing stagnation occurred within the sensor's boundaries. The stagnation sensor was used to verify the stagnation point measured using the

Table 2. Pressure Port Locations

Port	x/c for —															
	Flights 1 and 2 (baseline) with —				Flights 3–7 with —				Flights 8–10 with —				Flights 11 and 12 with —			
	Outboard belt of 0.0625 in.		Inboard belt of 0.0625 in.		Outboard belt of 0.0625 in.		Inboard belt of 0.0625 in.		Outboard belt of 0.0625 in.		Inboard belt of 0.1250 in.		Outboard belt of 0.0625 in.		Inboard belt of 0.1875 in.	
	US	LS	US	LS	US	LS	US	LS	US	LS	US	LS	US	LS	US	LS
Control	0.0000	0.0000	0.0000	0.0000	0.0000	0.0000	0.0000	0.0000	0.0000	0.0000	0.0000	0.0000	0.0000	0.0000	0.0026	0.0027
1	0.0062	0.0015	0.0062	0.0015	0.0062	0.0015	0.0062	0.0015	0.0062	0.0015	0.0062	0.0015	0.0062	0.0015	0.0057	0.0063
2	0.0098	0.0025	0.0098	0.0025	0.0098	0.0025	0.0098	0.0025	0.0098	0.0025	0.0098	0.0025	0.0098	0.0025	0.0112	0.0116
3	0.0165	0.0065	0.0165	0.0065	0.0165	0.0065	0.0165	0.0065	0.0165	0.0065	0.0165	0.0065	0.0165	0.0065	0.0127	0.0022
4	0.0276	0.0159	0.0276	0.0159	0.0276	0.0159	0.0276	0.0159	0.0276	0.0159	0.0276	0.0159	0.0276	0.0159	0.0139	0.0325
5	0.0383	0.0250	0.0383	0.0250	0.0383	0.0250	0.0383	0.0250	0.0383	0.0250	0.0383	0.0250	0.0383	0.0250	0.0421	0.0427
6	0.0499	0.0344	0.0499	0.0344	0.0499	0.0344	0.0499	0.0344	0.0499	0.0344	0.0499	0.0344	0.0499	0.0344	0.0522	0.0528
7	0.0602	0.0435	0.0602	0.0435	0.0602	0.0435	0.0602	0.0435	0.0602	0.0435	0.0602	0.0435	0.0602	0.0435	0.0725	0.0629
8	0.0706	0.0532	0.0706	0.0532	0.0706	0.0532	0.0706	0.0532	0.0706	0.0532	0.0706	0.0532	0.0706	0.0532	0.1065	0.0931
9	0.0811	0.0626	0.0811	0.0626	0.0811	0.0626	0.0811	0.0626	0.0811	0.0626	0.0811	0.0626	0.0811	0.0626	0.1529	0.1529
10	0.0922	0.0726	0.0922	0.0821	0.0922	0.0821	0.0922	0.0821	0.0922	0.0821	0.0922	0.0821	0.0922	0.0821	0.3033	0.3033
11	0.1014	0.0821	0.1014	0.1164	0.1014	0.1164	0.1014	0.1164	0.1014	0.1164	0.1014	0.1164	0.1014	0.1164	0.4037	0.4037
12	0.1126	0.0917	0.1126	0.1651	0.1126	0.1651	0.1126	0.1651	0.1126	0.1651	0.1126	0.1651	0.1126	0.1651	0.5791	0.5791
13	0.1380	0.1164	0.1380	0.2149	0.1380	0.2149	0.1380	0.2149	0.1380	0.2149	0.1380	0.2149	0.1380	0.2149	0.6793	0.6793
14	0.1634	0.1407	0.1634		0.1634		0.1634		0.1634		0.1634		0.1634		0.8045	0.8045
15	0.1902	0.1651	0.1902		0.1902		0.1902		0.1902		0.1902		0.1902		0.9045	0.9045
16	0.2413	0.1909	0.2413		0.2413		0.2413		0.2413		0.2413		0.2413		0.9545	0.9545
17	0.2668	0.2149	0.2668		0.2668		0.2668		0.2668		0.2668		0.2668		0.9745	0.9745
18	0.2918	0.3741	0.2918		0.2918		0.2918		0.2918		0.2918		0.2918		0.9845	0.9845
19	0.3162	0.4247	0.3162		0.3162		0.3162		0.3162		0.3162		0.3162		0.9945	0.9945
20	0.3412	0.4760	0.3412		0.3412		0.3412		0.3412		0.3412		0.3412			
21	0.3662	0.5501	0.3662		0.3662		0.3662		0.3662		0.3662		0.3662			
22	0.3912	0.6157	0.3912		0.4155		0.4155		0.4155		0.4155		0.4155			
23	0.4155	0.6490	0.4667		0.4667		0.4667		0.4667		0.4667		0.4667			
24	0.4418	0.6982	0.5172		0.5172		0.5172		0.5172		0.5172		0.5172			
25	0.4667	0.7423	0.5918		0.5918		0.5918		0.5918		0.5918		0.5918			
26	0.4917	0.7967	0.0706		0.0706		0.6421		0.6421		0.6421		0.6421			

Table 2. Concluded

Port	x/c for —													
	Flights 1 and 2 (baseline) with —		Flights 3–7 with —				Flights 8–10 with —				Flights 11 and 12 with —			
	Outboard belt of 0.0625 in.		Inboard belt of 0.0625 in.		Outboard belt of 0.0625 in.		Inboard belt of 0.1250 in.		Outboard belt of 0.0625 in.		Inboard belt of 0.1875 in.		Outboard belt of 0.0625 in.	
	US	LS	US	LS	US	LS	US	LS	US	LS	US	LS	US	LS
27	0.5172	0.8461	0.6669				0.6669							
28	0.5670	0.8955	0.6923				0.6923							
29	0.5918	0.9143	0.7171				0.7171							
30	0.6173	0.9442	0.7678				0.7678							
31	0.6421	0.9644	0.7933				0.7933							
32	0.6669	0.9741	0.8182				0.8182							
33	0.6923		0.8700				0.8700							
34	0.7171		0.8943				0.8943							
35	0.7678		0.9211				0.9211							
36	0.7933		0.9473				0.9473							
37	0.8182		0.9722				0.9722							
38	0.8700		0.9927				0.9927							
39	0.8943		1.0025				1.0025							
40	0.9211		1.0075				1.0075							
41	0.9473													
42	0.9722													
43	0.9927													
44	1.0025													
45	1.0075													

Table 3. Summary of Measurements List

Flight parameter	Range	Sample rate, Hz	Accuracy, percent FS
Normal acceleration (positive up), <i>g</i> units	−1 to 3	6	1
Lateral acceleration (positive right), <i>g</i> units	−1 to 1	6	1
Longitudinal acceleration (positive forward), <i>g</i> units	−1 to 1	6	1
Right wing angle of attack, deg	−10 to 30	2	1
Left wing angle of attack, deg	−10 to 30	2	1
Right wing angle of sideslip, deg	−20 to 20	2	0.8
Left wing angle of sideslip, deg	−20 to 20	2	0.8
Static pressure, psia	0 to 15	6	0.8
Dynamic pressure, ^a psid	0 to 1	6	1
Air temperature, °F	−30.9 to 104.7	6	0.8
Rudder (positive TE left), deg	−27.5 to 27	6	2
Aileron right, deg	−28.6 to 16.4	6	2
Stabilator, deg	−11.5 to 9	6	2
Pitch rate, deg/sec	−60 to 60	6	0.8
Roll rate, deg/sec	−60 to 60	6	0.8
Yaw rate, deg/sec	−60 to 60	6	0.8
True airspeed right, ^a knots	45 to 269	2	1.2
True airspeed left, ^a knots	45 to 269	2	1.2
Pressure ports 1–73, psid	−2.5 to 2.5	6	0.8
Center heated elements 1–20, volts	−2.5 to 2.5	DC	0.8

^aDerived parameters.

pressure-belt technique. A more detailed description of the sensor is found in appendix B.

Rate gyros and sensors, such as the angle of attack and sideslip sensors, were checked and calibrated. Typically, the pressure belts were visually inspected only if previous flight data indicated a blocked tube. To clear a blockage, the blocked tube was disconnected from the pressure multiplexer and a high-pressure stream of air was forced into the tube, either pushing the material out or downstream of the pressure port. The flow stagnation sensor was checked by passing a stream of air over the elements while observing the signal response. Flight data were recorded on a 10-track analog tape recorder. This system can record both pulse-code-modulated and frequency-modulated data.

Flight Test Procedure

Steady level flight tests were conducted at pressure altitudes of 4500, 5500, 6500, and 8500 ft. The steady test points were set at maximum cruise speed: 105, 95, 87, 78, and

70 knots, and “stall-warning” speed (fig. 7). Maximum cruise speed varied from 117 to 129 knots, depending on airplane weight and atmospheric conditions. The aircraft’s stall-warning sensor activated between 62 and 68 knots, 4 to 8 knots above the stall. Steady-state test-point data were recorded for 30 sec while the flight test engineer documented significant events for later interpretation and analysis of the data. After the test flight, the instrumentation technician inspected the pressure belts, flow stagnation, and airspeed sensors for any insect contamination or damage.

Computational Method

A computational investigation of tube size on pressure distribution was conducted using the two-dimensional Multielement Streamtube Euler Solver (MSES) code (ref. 4). MSES is the multi-element version of ISES (Inviscid Streamtube Euler Solver) and is developed to simultaneously solve, via Newton’s method, the coupled streamline-based Euler equations and the boundary-layer equations. The true airfoil

coordinates of the test section (plus the additional thickness due to the belt and the adhesive) were used to generate a grid for the Euler solver. The technique for measuring the true airfoil coordinates is described in appendix C. The flight conditions for the test points were used as inputs to the computational code. Once the grid was generated, the angle of attack and the flow conditions in terms of Reynolds number and Mach number were input into the MSES program to obtain the computed data. Initially, test points for the comparative analysis were to be matched by flight conditions in terms of angle of attack, Mach number, and Reynolds number; however, the airspeed calibration (appendix D) indicated that the angle-of-attack readings from the flow-direction sensors did not provide an acceptable level of repeatability (appendix E). The aircraft lift coefficient was therefore used for matching test points. For steady, level flight conditions the lift coefficient was calculated from equation (1).

$$C_L = \frac{2W}{\rho V^2 S} \quad (1)$$

Results

The data analysis includes a separate examination of the flight data as well as a comparison of the two-dimensional computational flight data with results based on the aerodynamic simulation program, MSES (ref. 4). Test points were chosen to cover a range of flight conditions spread across the flight envelope of the research airplane. The three lift coefficients selected (0.518, 0.824, and 1.131) encompassed an airplane angle-of-attack range between approximately 2.5° and 10.0° . Table 4 summarizes the test-point conditions for each figure in this section.

Finally, the outboard pressure belt was used as a reference for matching inboard pressure profiles for the various tube sizes. These profiles were used to verify and compare selected test points in terms of pressure loading.

Flight Test

The number of pressure ports was limited to the number of tubes that would fit in the test

section outboard of the propeller slipstream. Pressure distribution profiles for both the 0.0625- and 0.1250-in. OD tubing consisted of data from a total of 52 upper and lower surface pressure ports. For the 0.1875-in. OD tubing profile, 30 ports were used. Table 2 lists detailed information on the number of tubes and belt sizes. The reduction in the number of pressure ports available with the 0.1875-in. tubing made the resulting pressure profiles more difficult to interpret than with the data taken with the tubing of small diameters.

Figures 8, 9, and 10 show flight data for the three tube sizes at the three lift coefficients. At the lowest lift coefficient, $C_L = 0.518$ and a Mach number of $M_\infty = 0.16$ (fig. 8), there was excellent agreement among the data for all three tube sizes. All sizes captured the stagnation point; however, the results for the 0.0625-in. OD (thinnest) tubing indicated slightly more pressure recovery at the trailing edge. Figure 9 shows the flight data for $C_L = 0.824$ at $M_\infty = 0.13$. Although the three data sets were in fair agreement, there were noticeable discrepancies at both the leading edge and trailing edge, and only the 0.0625-in. OD tubing captured the stagnation point. The minimum pressure coefficient, $C_{p,\min}$, is nearly identical for the three tube sizes. Again, the thinnest tubing indicated more pressure recovery at the trailing edge. Figure 10 shows that the three data sets for $C_L = 1.131$ at $M_\infty = 0.11$ had nearly identical $C_{p,\min}$. At these conditions, none of the three tube sizes captured the stagnation point. Trailing-edge flow behavior for $C_L = 1.131$ is similar to the $C_L = 0.824$ data set (fig. 9); also, the pressure coefficient of the trailing edge, $C_{p,te}$, for the thinnest tubing is nearly zero for both conditions. Overall, there was fair agreement; however, the differences among the measured pressures for the three tube sizes increase with increasing angle of attack.

Computational Analysis

Various flight conditions were investigated using the MSES code and the true airfoil coordinates, accounting for variations in belt thickness due to the difference in tubing outer diameter and adhesive material.

Table 4. Test-Point Summary

[NA is not applicable]

Fig.	α	α (2D)	Lift coefficient	Mach number	Reynolds number	Flight data			Computational data				
						0.625-in. tubing	0.1250-in. tubing	0.1875-in. tubing	0.0625-in. tubing (a)	0.1250-in. tubing (a)	0.1875-in. tubing (a)	True airfoil (b)	NACA airfoil (c)
8	(d)	NA	0.518	0.16	(d)	X	X	X					
9	(d)	NA	0.824	0.13	(d)	X	X	X					
10	(d)	NA	1.131	0.11	(d)	X	X	X					
11	NA	3.30	0.518	0.16	4.80×10^6				X	X	X	X	
12	NA	6.60	0.824	0.13	3.75×10^6				X	X	X	X	
13	NA	9.00	1.131	0.11	3.22×10^6				X	X	X	X	
14	NA	6.60	0.824	0.13	3.75×10^6				X			X	
15	NA	6.60	0.824	0.13	3.75×10^6					X		X	
16	NA	6.60	0.824	0.13	3.75×10^6						X	X	
17	NA	3.30	0.518	0.16	4.80×10^6							X	X
18	3.5	3.30	0.518	0.16	4.80×10^6	X			X				
19	2.7	3.30	0.518	0.16	4.95×10^6		X			X			
20	2.8	3.30	0.518	0.16	4.53×10^6			X			X		
21	6.5	6.60	0.824	0.13	3.75×10^6	X			X				
22	6.4	6.60	0.824	0.13	3.90×10^6		X			X			
23	7.0	6.60	0.824	0.13	3.90×10^6			X			X		
24	9.0	9.00	1.131	0.11	3.22×10^6	X			X				
25	9.7	9.00	1.131	0.11	3.70×10^6		X			X			
26	9.1	9.00	1.131	0.11	3.10×10^6			X			X		

^aComputational data based on true airfoil coordinates.^bAirfoil coordinates measured from existing wing.^cCoordinates based on ideal shape.^dRefer to plot for detailed information.

In figures 11, 12, and 13 a comparison of the computed pressure distributions for the three tube sizes is shown for the three selected airplane lift conditions. At a two-dimensional angle of attack of 3.3° (fig. 11), the comparison indicates only a minimal difference among the predicted pressure distribution for the various tube diameters. This was also the angle at which the predicted pressure distribution data most closely matched the flight-measured pressure distribution at an aircraft lift coefficient of 0.518. The predicted pressures at the angles of attack of 6.6° and 9.0° most closely matched the flight-measured pressure distributions at lift coefficients of 0.824 and 1.131, respectively. At these mid and high aircraft lift coefficients (figs. 12 and 13), the suction peak increased slightly with the increase in tube diameter; however, in all cases the true airfoil exhibited the highest suction pressure level. In figures 14, 15, and 16, the MSES-predicted pressure variations for the true airfoil and the true airfoil with each of the three additional tubing thicknesses are plotted for a lift coefficient of 0.824.

Discussion

Overall, the pressure-belt technique was shown to be reliable and to work well in the flight environment. The technique provided very consistent surface-pressure data, and the flight-measured pressure distributions for the three tube sizes at the selected test conditions (obtained during different flights) were in good agreement, as shown in figures 8 through 10. Some chord-wise waviness in the pressure distributions was seen consistently throughout the range of lift coefficients. The most noticeable difference among the pressure data with the three tubing sizes occurred in the trailing-edge region, where the thickest tubing (0.1875-in. OD) appeared to have the most pronounced effect on the pressure distribution. The data also showed that at the lowest lift coefficient ($C_L = 0.518$) there was very little difference among the measured pressure distributions of the three tube sizes.

The computational results, obtained with the two-dimensional flow analysis method MSES,

showed only slight differences in the pressure distributions due to the various tube sizes (figs. 11 through 16). Particularly at the lowest angle of attack ($\alpha = 3.3^\circ$), differences among the pressure distributions for the three belt sizes are very small. At the mid and high angle-of-attack conditions, the MSES code predicted slightly lower pressures downstream of the leading edge, particularly for the thickest tubing. The suction peak for the true airfoil is consistently slightly higher than those of the true airfoil with tubing at all three lift conditions. Figure 17 shows a comparison of the computed pressure data for the true (actual) airfoil, based on measured airfoil coordinates, and for a modified NACA 652-415 airfoil (personal communication with Trevor Linton-Smith of Pipe Aircraft Corporation, October 7, 1980). Similar to the measured pressure distributions, MSES predicted the pressure perturbations due to a forward-facing step on the wing surface that can be seen downstream of the 40-percent chord station on the lower and upper surfaces. Other discrepancies seen in the pressure distributions are the result of slight differences between the geometry of the true airfoil and that of the NACA airfoil. For example, the flap-gap fairing also caused some waviness in the pressure distribution at approximately 80-percent chord station.

Figures 18, 19, and 20 show individual test-point comparisons among the flight and computed data for the three tube sizes at an aircraft lift coefficient of 0.518 and a Mach number of 0.16. As explained earlier, the measured surface pressures are compared with computed data by selecting the best match of the surface-pressure distribution profile at a two-dimensional angle of attack. There is a close agreement among the measured and computed pressure distributions; however, the two-dimensional flow analysis method does not predict the trailing-edge flow behavior very well for the airfoil with belt. Note that the waviness in the pressure data is well predicted by MSES and, thus, clearly caused by surface waviness in the true airfoil. Flight and computed pressure distributions for the three tube diameters at a lift coefficient of 0.824 and a Mach number of 0.13 (figs. 21, 22, and 23) are in fair agreement. The thinnest tubing captured the

stagnation point, and overall, was most similar to the computed data (fig. 21). At the highest lift coefficient, $C_L = 1.131$ and a Mach number of 0.11 (figs. 24, 25, and 26), MSES consistently predicted a lower value for $C_{p,\min}$ than that measured in flight. This discrepancy in the leading-edge pressures appears to be linked to the trailing-edge flow. At this high-lift condition, the pressure-belt data showed nearly zero pressure gradient at the trailing-edge region for all three cases. Although zero pressure gradient in the trailing-edge region is generally linked to flow separation, in this case flow separation does not appear the cause.

Several factors might have contributed to the slight discrepancies in the pressure measurements. The spanwise flow pushed up by the belt could have caused a local drop in pressure at the belt edges, particularly in the trailing-edge region where this effect can be more significant with increasing angle of attack. In an attempt to minimize this effect, dummy tubes were added to both sides of the belt and faired with the adjacent wing surface. The fact that the surface of the pressure belt in the spanwise direction is corrugated may be a contributing factor in the pressure drop over the belt surface. It also appears that the installation method used to secure the ends of the pressure belt, located at the trailing edge, to the wing surface might have contributed to the drop in pressure at this location. These data indicate that some of the error in the pressure measurement could be reduced by selecting the thinnest belt tubing available. To reduce the error even further, the entire belt surface should be smoothed before drilling the pressure ports, an effort that may negate some of the time saving advantages of the pressure-belt technique. The belt installation method used to seal and secure the trailing edge could have been greatly improved. Results show that the more robust and intrusive trailing-edge bonding was not necessary, and that minimal bonding compound and edge fairing would have likely yielded better results.

Conclusions

Flight tests were conducted at the NASA Langley Research Center to investigate the effects

of pressure-belt tube size on measured pressure distributions. A light general aviation aircraft was instrumented with two pressure belts. The outboard belt was constructed from 0.0625-in. OD tubing and served as the baseline configuration. Three tube sizes were tested on the inboard belt: 0.0625-, 0.1250-, and 0.1875-in. OD. A comparison was made among pressure distributions obtained from the three tube sizes at three different airplane lift coefficients. The measured pressure data were also compared with two-dimensional computed pressure distributions predicted by the viscous-flow code for airfoils.

At low-lift conditions, $C_L = 0.518$, all three tube sizes measured nearly identical pressures along the wing chord. Small discrepancies in the measured pressures could be noted near the trailing edge with the pressure discrepancies increasing with increasing tube diameter. The measured pressures showed good agreement with the computed pressures except near the trailing edge, where the predicted pressures were slightly higher than the measured pressures. Larger discrepancies in measured pressures among different tubing sizes occurred mainly in the trailing-edge region at mid-lift and high-lift conditions ($C_L = 0.824$ and $C_L = 1.131$, respectively). Also, the discrepancies between computed and measured pressures became larger with increasing tube diameter and increasing lift coefficient.

Several possible error sources have been identified regarding the discrepancies in the pressure distribution measurements: spanwise flow, tubing size, and installation method. Recommendations for increasing the likelihood of obtaining meaningful and significant data using pressure belts are as follows:

1. Tube size and adhesive thickness. Select the thinnest tubing available that will provide for your installation technique and test requirements. It is also important to select the appropriate adhesive. It should be as thin as possible, yet maintain the required bonding strength.
2. Surface smoothing. It is best to use an aerodynamic smoothing compound to

blend the pressure belt with wing surface without adding additional thickness to the belt or wing. This effort may negate some of the time-saving advantages of the pressure-belt technique.

3. Careful installations. Use extreme care when installing the pressure belts, particularly in the trailing-edge region. The pressure belt should precisely conform to the

actual surface, avoiding any raised or crimped tubing.

4. Unobstructed pressure ports. It is important to ensure that each port has a clean, even pressure hole with no obstructions or burrs to impede airflow. It is recommended that each hole be inspected using a magnifying instrument during the hole fabrication process as well as during the systems preflight check.

Appendix A

Research Airplane

An all-metal, four-place, low-wing airplane with retractable, tricycle-type landing gear served as the test airplane for the flight evaluation of the pressure belts and flow stagnation sensor. The airplane is shown in figure A1 and its physical characteristics are listed in table A1. The airplane is powered by a four-cylinder, horizontally opposed, reciprocating engine that has a rated power at sea level of 200 hp and is equipped with a constant speed propeller. The airplane flight envelope includes airspeeds up to 150 knots and a service ceiling of 15 000 ft. For these experiments, the airplane was flown at four altitudes between 4500 and 8500 ft over an indicated airspeed range from 62 to 126 knots. The wing is semitapered and has a span and aspect ratio of 35.43 ft and 7.24, respectively. Measurements were made on the inboard constant-chord panel of the right wing. The nominal airfoil section at this location is an NACA 65₂-415 and the chord length is 5.25 ft. A smooth continuous surface for mounting the pressure belts was achieved by

locking the flaps in the zero position, filling the space between the wing and the flap with foam, and then covering the foam with an aluminum foil tape.

The two aft seats were removed to accommodate an instrumentation pallet. The pallet carried the data recorder, power supply, and associated instrumentation required for recording the Pulse Code Modulated (PCM) data.



Figure A1. Research airplane.

Table A1. Airplane Physical Characteristics

Overall dimensions:

Span, ft	35.43
Length, ft	27.80
Height, ft (measured at vertical tail)	8.26

Powerplant:

Type	Reciprocating, four-cylinder, horizontally opposed, Lycoming IO-360-C1C6
Rated power at sea level, hp	200
Rated continuous speed, rpm	2700

Propeller:

Type	Two bladed, constant speed
Diameter, in.	76
Pitch (variable), deg	14 to 31

Wing:

Area, ft	173.7
Span, ft	35.43
Root chord, in.	74.0
Chord of constant section, in.	63.0
Tip chord, in.	42.2
Mean aerodynamic chord, in.	62.16
Aspect ratio	7.24
Dihedral, deg	7.0
Incidence at root, deg	2.0
Incidence at tip, deg	-1.0
Airfoil section (constant chord region)	NACA 65 ₂ -415

Flap:

Area (each), ft	7.3
Span, in.	85.50
Chord, in.	12.2
Deflection, deg	20.0

Aileron:

Area (each), ft ²	6.95
Span, in.	100.05
Mean chord, in.	10.01
Deflection, deg	30 up, 16 down

Stabilator:

Area (including tab), ft ²	25.0
Chord (constant), in.	30.0
Deflection, deg	10 up, 10 down
Aspect ratio	4.0
Dihedral, deg	7.0
Hinge line, percent stabilator chord	27.97
Airfoil section	NACA 0012

Table A1. Concluded

Tab:

Area, ft ²	4.4
Span, in.	106.2
Chord (constant), in.	6.0
Tab hinge line to stabilator hinge line, in.	15.91

Vertical tail:

Area (including rudder), ft ²	17.6
Span, in.	60.84
Root chord, in.	54.52
Tip chord, in.	28.62
Mean aerodynamic chord, in.	42.91
Aspect ratio.....	1.47
Leading-edge sweepback, deg	33.91

Rudder:

Area, ft ²	5.8
Span (parallel to hinge line), in.	61.6
Average chord aft of hinge line, in.	11.85
Deflection, deg	28 left, 28 right

Appendix B

Flow Stagnation Sensor

A small 2- by 2-in. flow stagnation sensor (FSS) was installed on the leading edge of the research airplane as shown in figure B1. Based on the tri-element design of Manuel, Carraway, and Croom (ref. 5), each measurement consisted of three parallel elements spaced 0.05 in. apart. The sensor had a total of 60 elements, allowing for 20 measurements with a 0.1-in. resolution. The center element of a measurement was heated using a constant temperature anemometer (CTA), as depicted in figure B2. The heat dissipating from each center element was convected to one of its surrounding elements downstream of the stagnation point. The surrounding elements were passively monitored by a bridge circuit using a resistive thermometer. The resistance of the downstream element increased under the influence of the heated flow, unbalancing the bridge circuit. The polarity of the output signal from the bridge determined the direction of the airflow. The area in which stagnation occurred was determined by the output of two adjacent measurements indicating opposite polarity.

Figures B3(a), B4(a), and B5(a) show the full-chord flight-measured pressure distributions at high, medium, and low aircraft lift coefficients. Corresponding leading-edge pressure distributions, including the stagnation regions, are shown in figures B3(b), B4(b), and B5(b). The regions of flow stagnation, as measured by both the FSS and the inboard pressure belt, are indicated by the shaded areas. The data from the thinnest outer diameter tubing, 0.0625-in. OD, were used for most of the comparative analysis in this appendix. For the three aircraft lift coefficients examined, there was good agreement between the region of stagnation as indicated by the FSS results and the pressure results. With the exception of the highest lift coefficient, the FSS region consistently fell within the pressure belt's measured stagnation region. Table B1 shows the pressure port locations and the corresponding flow stagnation sensor elements. The spacing between pressure ports was increased with increasing distance from

the leading edge. Thus, the resolution of the stagnation point, determined from the measured wing surface pressures, decreased with increasing lift coefficient as a result of the downstream shift of the stagnation point.

Table B1. Pressure Port Locations and Corresponding FSS Elements

Element	x/c	Tubing size, in., of—	
		0.625/0.1250	0.1875
	0.00000	X	X
1	0.00004		
2	0.00038		
3	0.00073		
	0.00260		X
	0.00570		X
	0.00620	X	
	0.00980	X	
	0.01120		X
	0.01270		X
4	−0.00030		
5	−0.00090		
	−0.00150	X	
6	−0.00160		
	−0.00220		X
7	−0.00240		
	−0.00250	X	
	−0.00270		X
8	−0.00280		
9	−0.00450		
10	−0.00580		
	−0.00630		X
	−0.00650	X	
11	−0.00710		
12	−0.00840		
13	−0.00980		
14	−0.01120		
	−0.01160		X
15	−0.01260		
16	−0.01410		
17	−0.01510		
	−0.01590	X	
18	−0.01660		
19	−0.01800		
20	−0.01940		
	−0.02500	X	
	−0.03500		X

Figure B3 shows data for $C_L = 0.36$, $M_\infty = 0.19$, and $\alpha = 1.5^\circ$. The pressure-belt data suggest that stagnation occurred between an x/c of 0.0 and 0.0025, whereas the FSS indicated stagnation between an x/c of 0.0016 and 0.0024. Figure B4 shows the pressure distribution data for $C_L = 0.84$, $M_\infty = 0.12$, and $\alpha = 6.3^\circ$. The region of stagnation detected by the FSS

(fig. B4(b)) was between an x/c of 0.0112 and 0.0126. The pressure belt showed stagnation occurred between an x/c of 0.0025 and 0.0159. Figure B5 shows pressure distribution data for $C_L = 1.15$, $M_\infty = 0.10$, and $\alpha = 8.6^\circ$. The FSS region was aft of x/c of 0.0200 and the maximum pressure measured with the pressure belt occurred between $x/c = 0.0025$ and 0.0159.

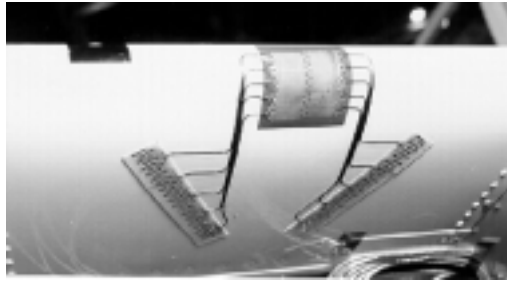


Figure B1. Flow stagnation and velocity sensor.

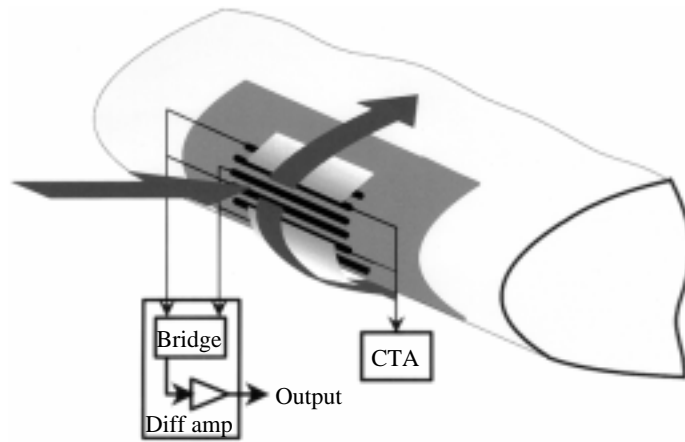
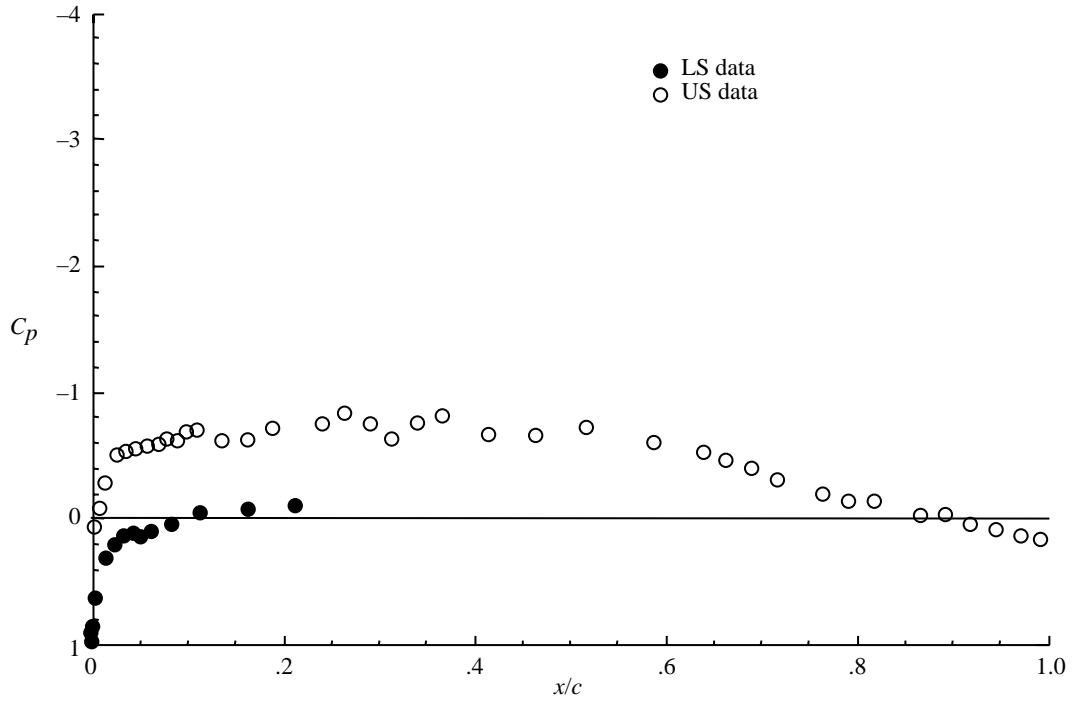
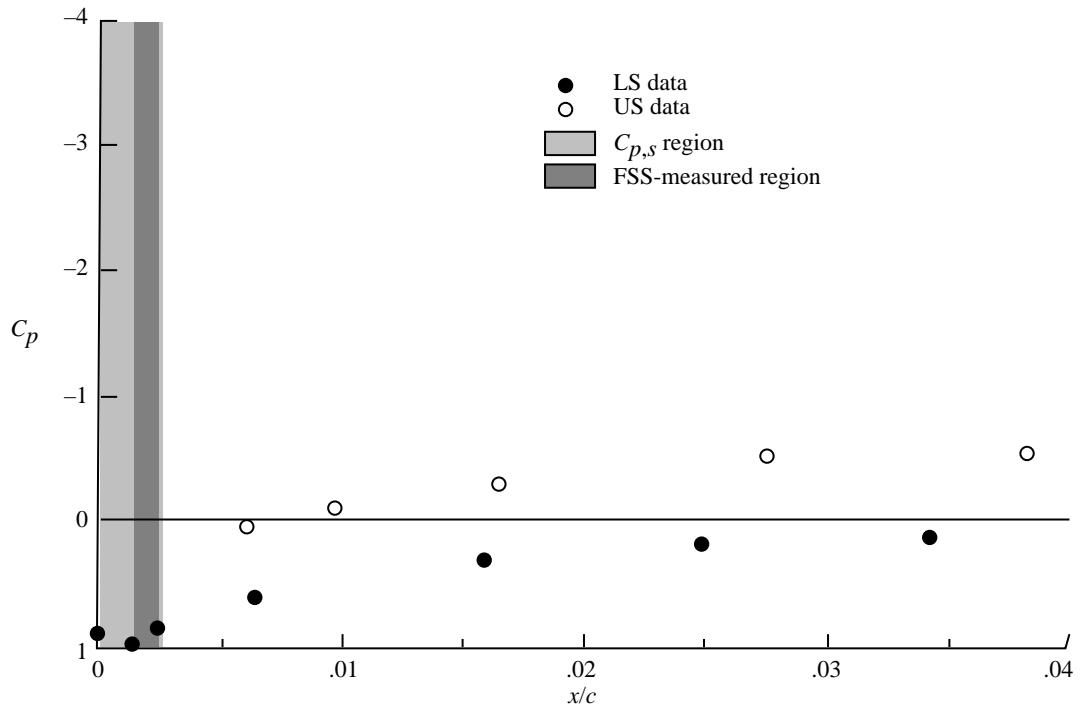


Figure B2. Schematic of flow stagnation and velocity sensor.

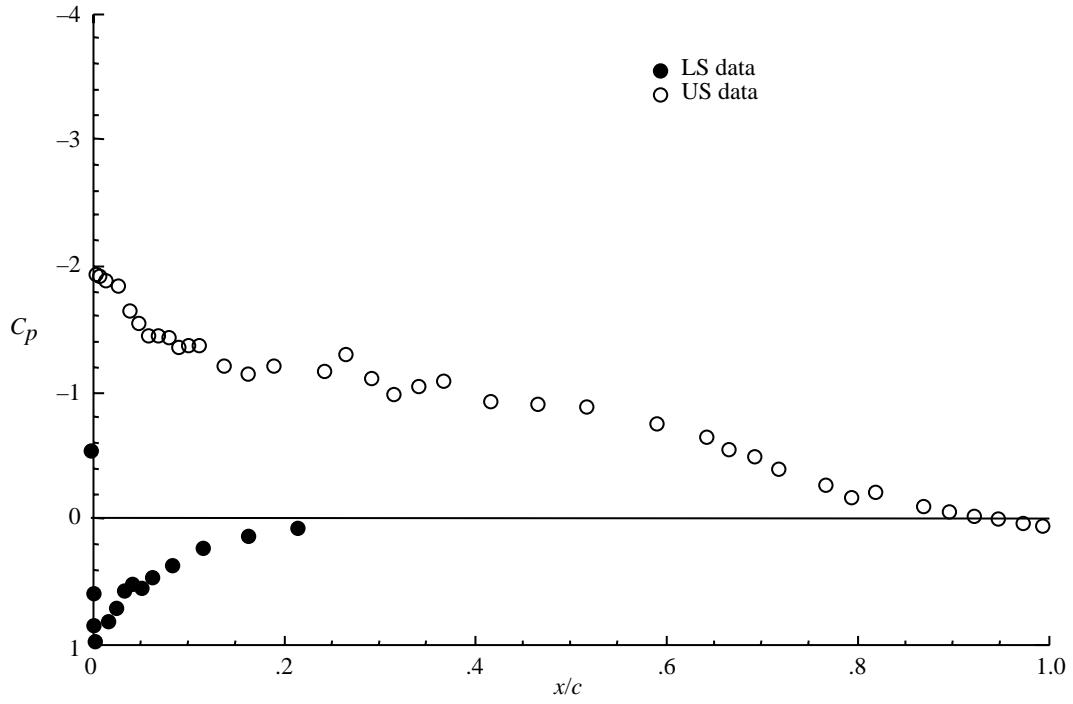


(a) Full-chord flight-measured.

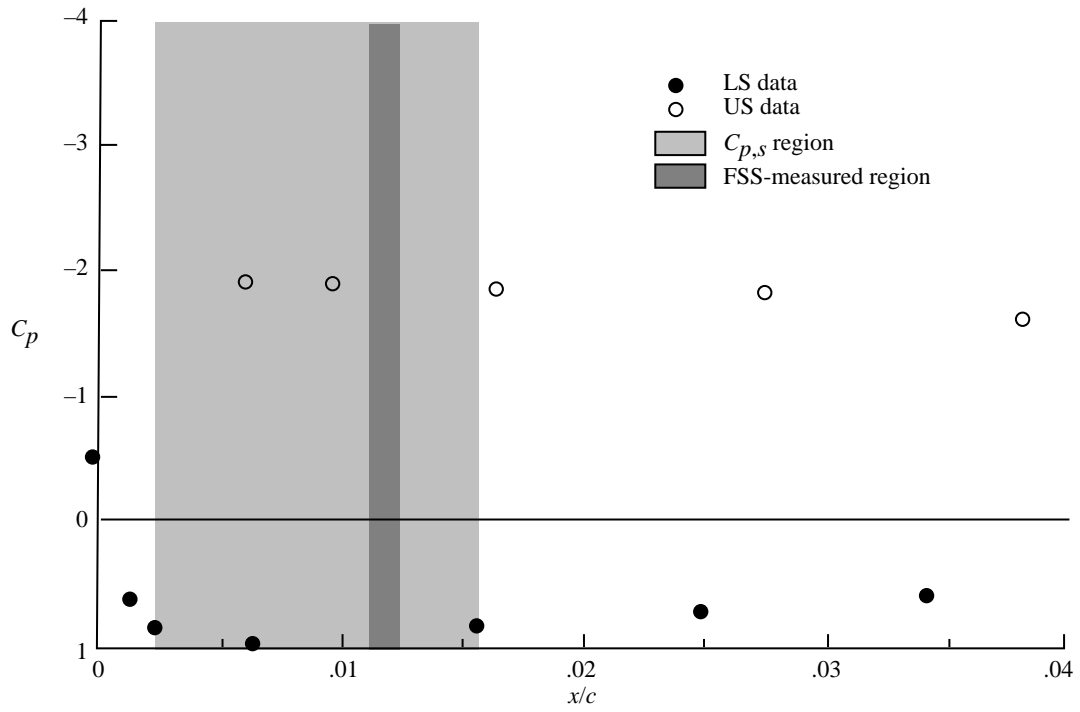


(b) Corresponding leading edge.

Figure B3. Measured pressure distribution data for $C_L = 0.36$, $M_\infty = 0.19$, $h = 6400$ ft, and $\alpha = 1.5^\circ$.

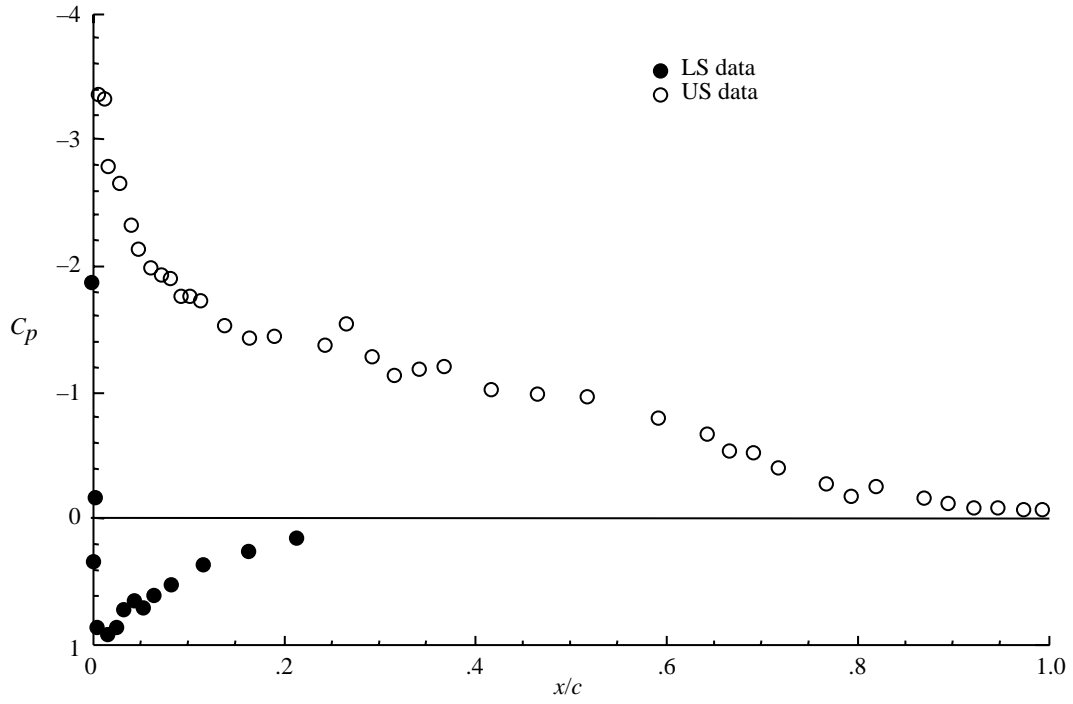


(a) Full-chord flight-measured.

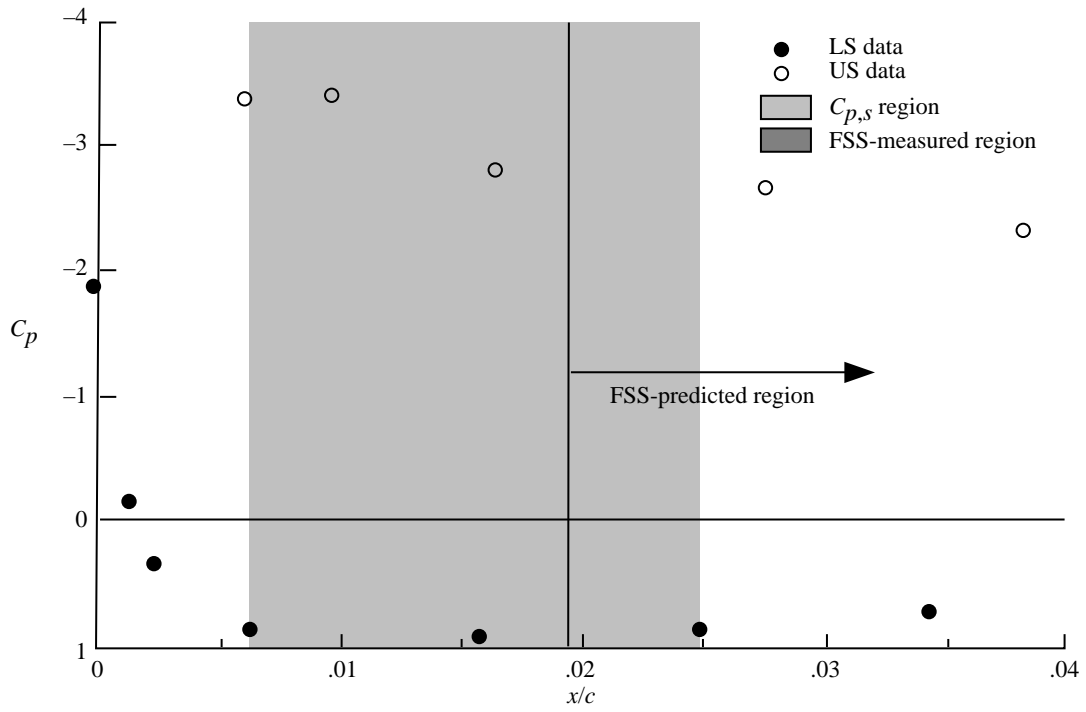


(b) Corresponding leading edge.

Figure B4. Measured pressure distribution and FSS data for $h = 6400$ ft, $M_\infty = 0.12$, $\alpha = 6.3^\circ$, and $C_L = 0.84$.



(a) Full-chord flight-measured.



(b) Corresponding leading edge.

Figure B5. Pressure distribution and FSS data for $h = 6400$ ft, $M_\infty = 0.10$, $\alpha = 8.6^\circ$, and $C_L = 1.15$.

Appendix C

Methodology for Obtaining Accurate Airfoil Coordinates

A wing contour template was made of the constant-chord section of the right wing of the research airplane in order to accurately define the true airfoil.

Two separate pieces of particle board were cut to the approximate shape of the upper and lower

wing surfaces. The airfoil forms were lined with a thin layer of clay and the two cutouts were again placed onto the wing surface in the chordwise direction (fig. C1). By applying slight pressure in a downward direction, an exact mold of the airfoil section was made. Once dry, the form was measured by a precision planer. The precision planer was capable of providing both x and z coordinates for up to 500 points. The coordinates were later used as input into the flow analysis program in order to generate a surface grid for the computational analysis.

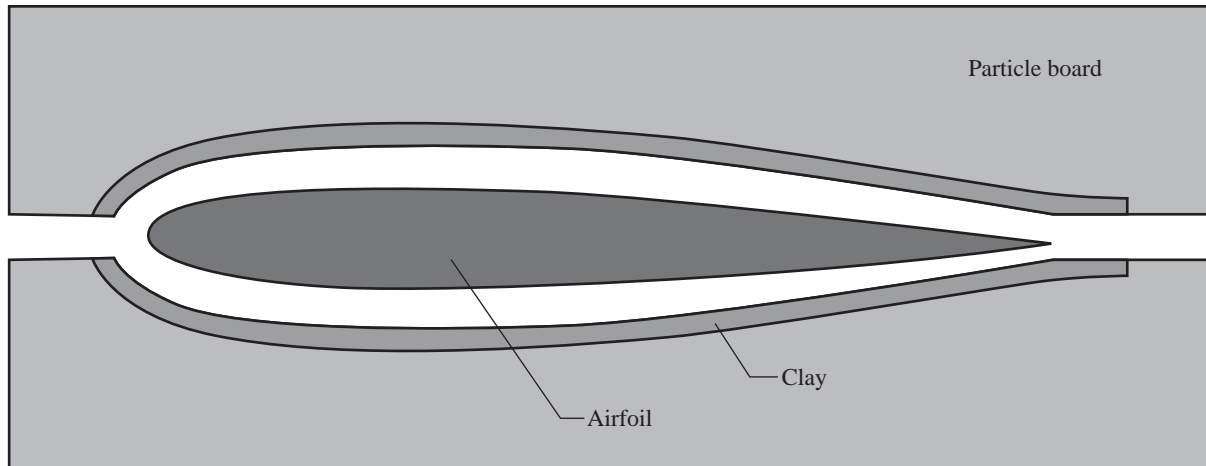


Figure C1. Wing contour template.

Appendix D

Airspeed Calibration Methodology

An in-flight airspeed calibration was conducted to evaluate the accuracy of the aircraft's pitot/static system and the wing-tip flow-direction sensors.

A "laser tracking" tower fly-by airspeed calibration (ref. 3) of the research airplane was conducted at the NASA Wallops Flight Facility (WFF). The ground-based laser measured the geometric height of the airplane, from which the pitot/static position error was derived. A pressure-height survey was conducted prior to launching the aircraft for the airspeed calibration. First, a balloon was released and tracked by laser to determine the wind profile up to 1100-ft above ground level at the test site. If the winds were less than 17 knots at 1100 ft, a tethersonde balloon was released to conduct a pressure survey. During the balloon's ascent to 700 ft, it was stopped every 100 ft to allow the laser to verify the balloon's altitude. From 700 to 1100 ft, the balloon was stopped every 50 ft for an altitude verification. After the balloon had taken data up to 1100 ft, it was retracted, stopping at the previously verified altitudes.

When the balloon survey was completed, the research airplane was launched. Test points covered the entire speed range and were flown between altitudes of 700 and 1100 ft. A post-flight pressure height survey was conducted in the same manner as the preflight survey.

Data for the balloon and laser were recorded inside the laser-tracking facility along with video tracking of the aircraft. These data and the flight data recorded onboard the research airplane were used to derive the static pressure position error.

Deriving the position error required that all unsteady data be filtered out of the extensive data base. Filtering was accomplished by selecting only those data sets in which the three angular rates and the longitudinal accelerations were near zero with an accompanying acceleration that remained close to a steady 1g condition. The steady-state data were then used to determine a calibration equation to correct the flight data for static pressure position error. Figure D1 shows a curve fit of $\Delta p/q$ versus corrected angle of attack.

The airspeed calibration derived using the laser-tracking tower-flyby technique was virtually identical to the aircraft manufacturer's calibration. The correction was applied to the appropriate aircraft and instrumentation data.

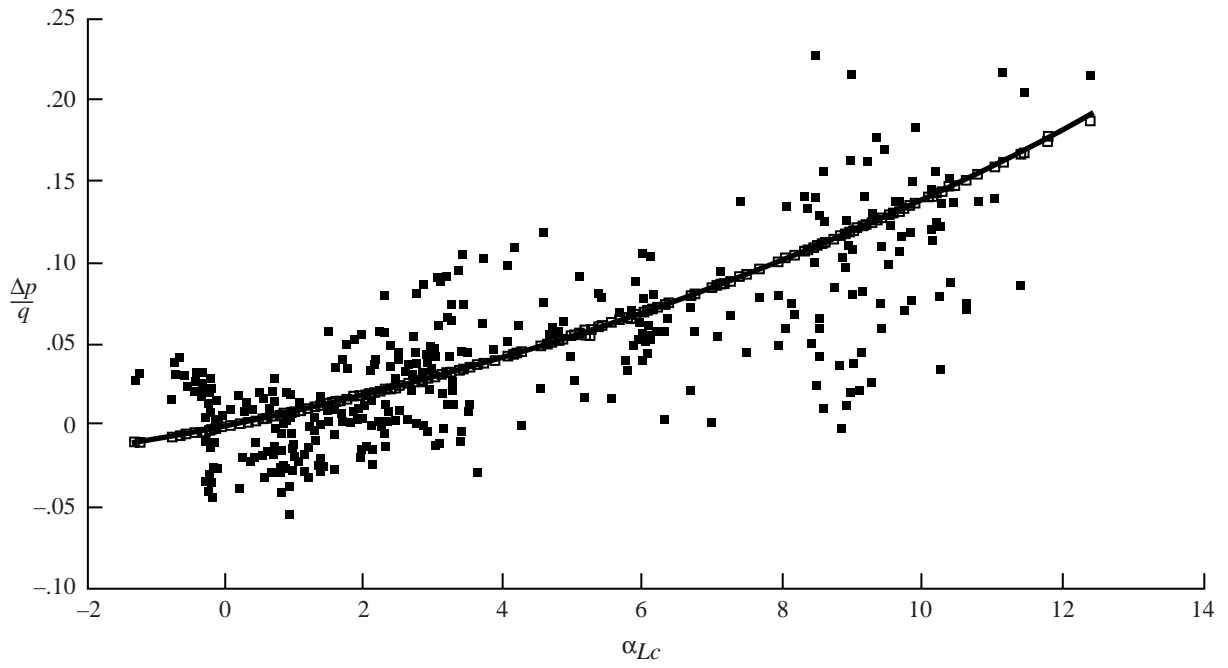


Figure D1. Curve fit of angle of attack versus pitch. $\frac{\Delta p}{q} = 0.00053\alpha_{Lc}^2 + 0.00846\alpha_{Lc} - 0.00067$.

Appendix E

Flow-Direction and Velocity Sensor

The research airplane was instrumented with two flow-direction and velocity sensors (figs. E1 and E2, ref. 6) designed to measure the angles of attack and sideslip, as well as true airspeed. These sensors were housed at the ends of both wing-tip booms, 3.92 ft forward from the wing's leading edge. The flow-velocity sensor was capable of measuring true airspeeds from 29.5 to

295 ft/sec. The angle-of-attack sensor had a measurement range of $\pm 120^\circ$ with a static accuracy of $\pm 0.35^\circ$ and the sideslip sensor had a range of $\pm 55^\circ$ and a static accuracy of $\pm 0.25^\circ$.

Results from the airspeed calibration indicated that the flow-direction sensors used for this project were not sufficiently accurate. Because of the significant errors, it was determined that the measured angle-of-attack values could not be used for data correlation; however, for completeness, the values are listed throughout the data analysis section.

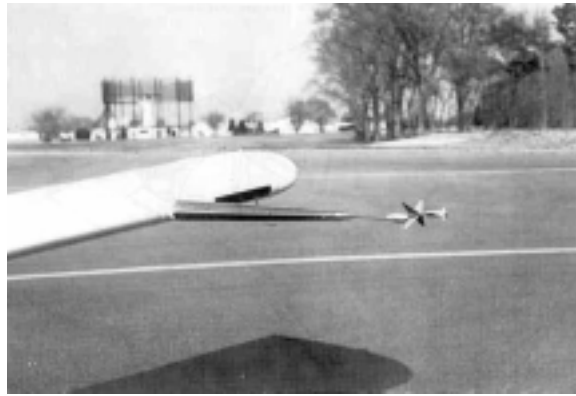


Figure E1. Flow direction and velocity sensor.

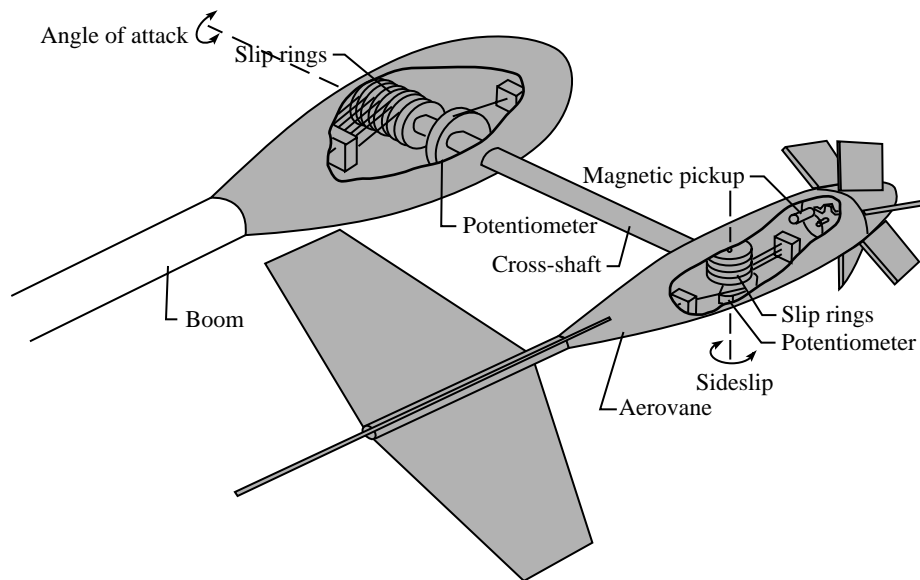


Figure E2. Flow direction and velocity sensor schematic.

References

1. Port, W. G. A.; and Morrall, J.: *Flight Tests of a Simple Method of Measuring Pressure Distributions on a Wing*. CP No. 422, British A.R.C., 1959.
2. Yip, L.; Vijgen, P. M.; Hardin, J. D.; and van Dam, C. P.: In-Flight Pressure Measurements on a Subsonic Transport High-Lift Wing Section. *J. Aircr.*, vol. 32, no. 3, May–June 1995, pp. 529–538.
3. Gracey, William: *Measurement of Aircraft Speed and Altitude*. NASA RP-1046, 1980.
4. Drela, Mark: Newton Solution of Coupled Viscous/Inviscid Multielement Airfoil Flows. AIAA-90-1470, June 1990.
5. Manuel, G. S.; Carraway, D. L.; and Croom, C. C.: The Laminar Separation Sensor: An Advanced Transition Measurement Method for Use in Wind Tunnel and Flight. SAE Paper 871018, Apr.–May 1987.
6. Kershner, David D.: *Miniature Flow-Direction and Airspeed Sensor for Airplanes and Radio-Controlled Models in Spin Studies*. NASA TP-1467, 1979.

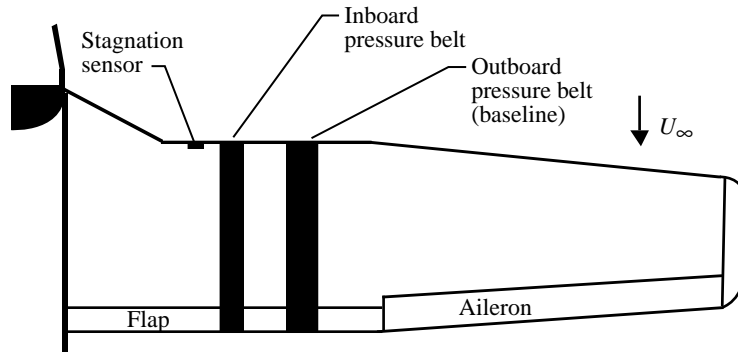


Figure 1. Wing instrumentation and belt configuration.

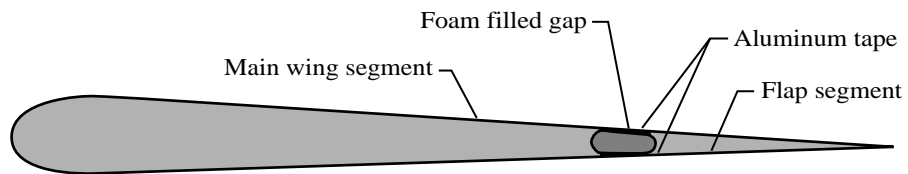


Figure 2. Wing modification.

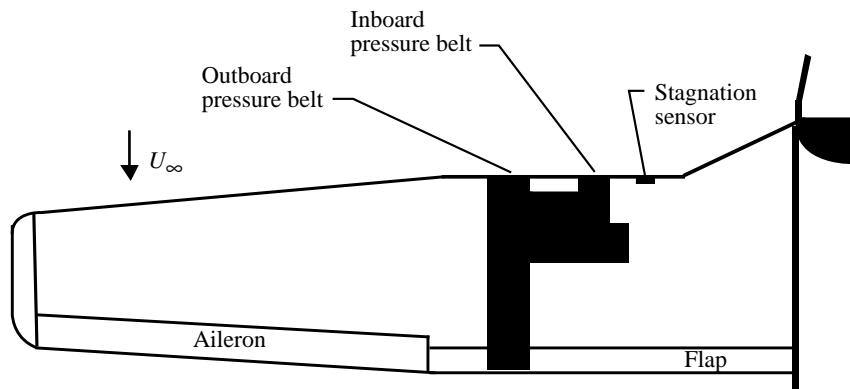


Figure 3. Pressure belt arrangement on lower wing surface.

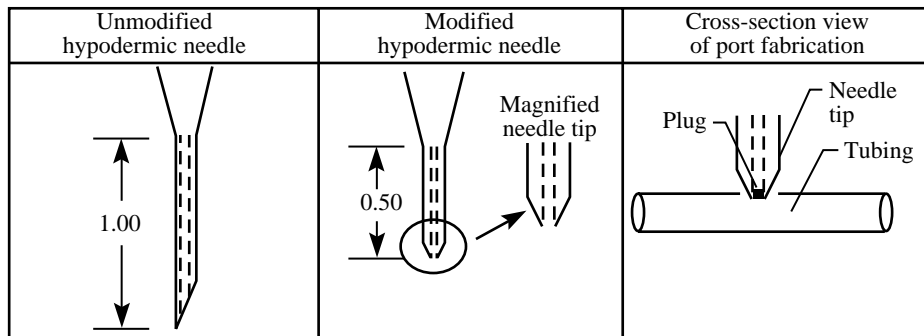


Figure 4. Needle modification. Dimensions are in inches.



Figure 5. ESP transducer.

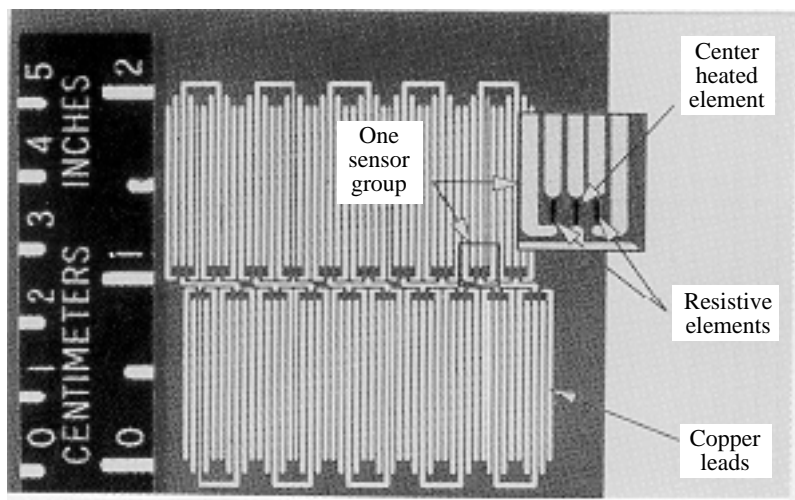


Figure 6. Flow stagnation sensor.

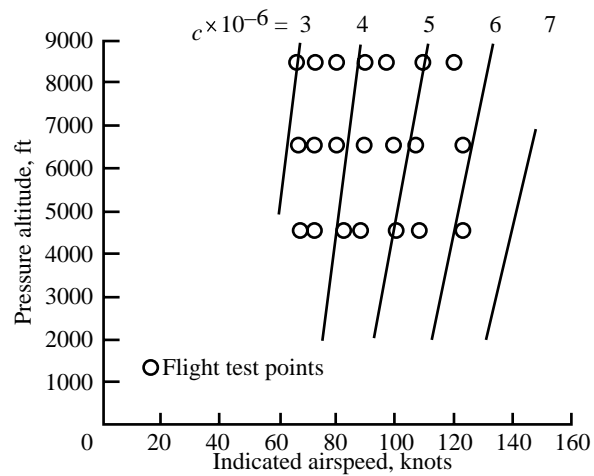


Figure 7. Steady level flight test points.

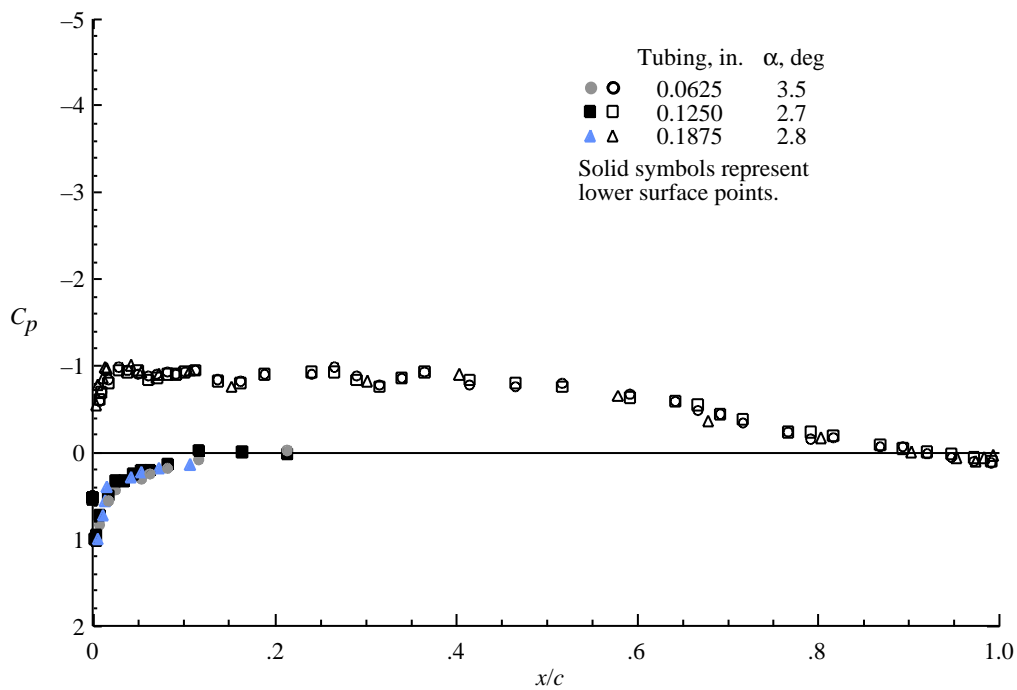


Figure 8. Flight pressure distribution data for $C_L = 0.518$ and $M_\infty = 0.16$.

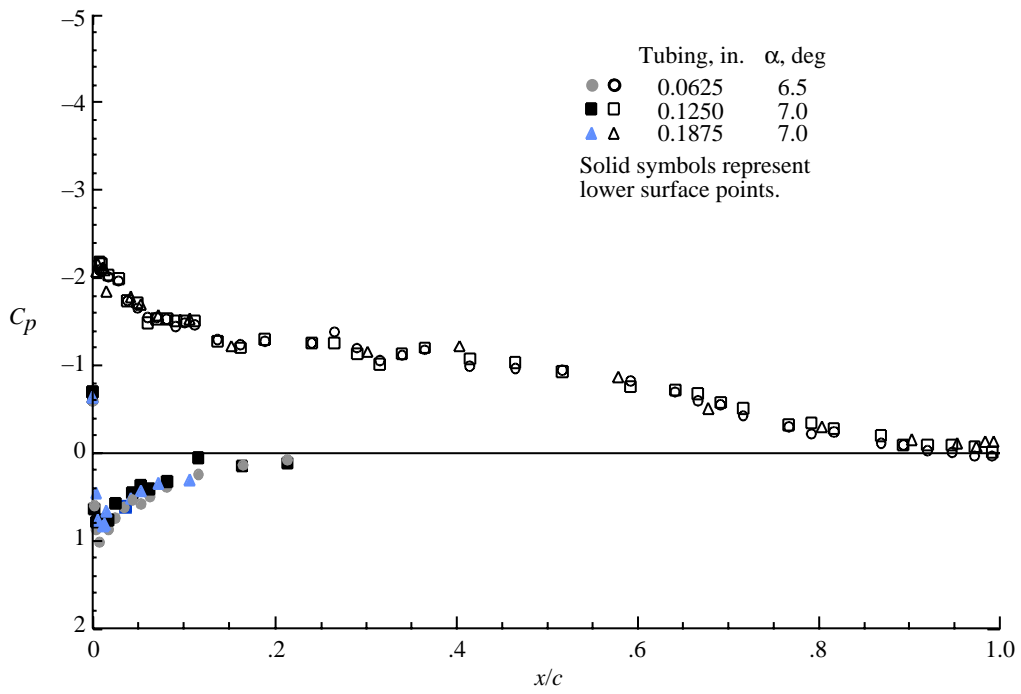


Figure 9. Flight pressure distribution data for $C_L = 0.824$ and $M_\infty = 0.13$.

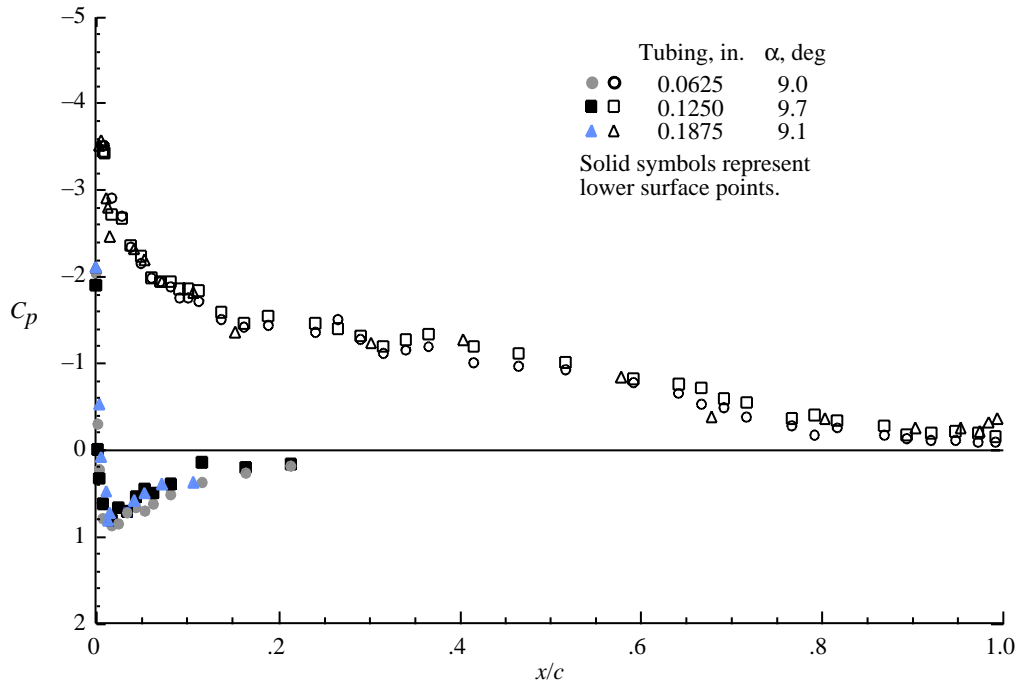


Figure 10. Flight pressure distribution data for $C_L = 1.131$ and $M_\infty = 0.11$.

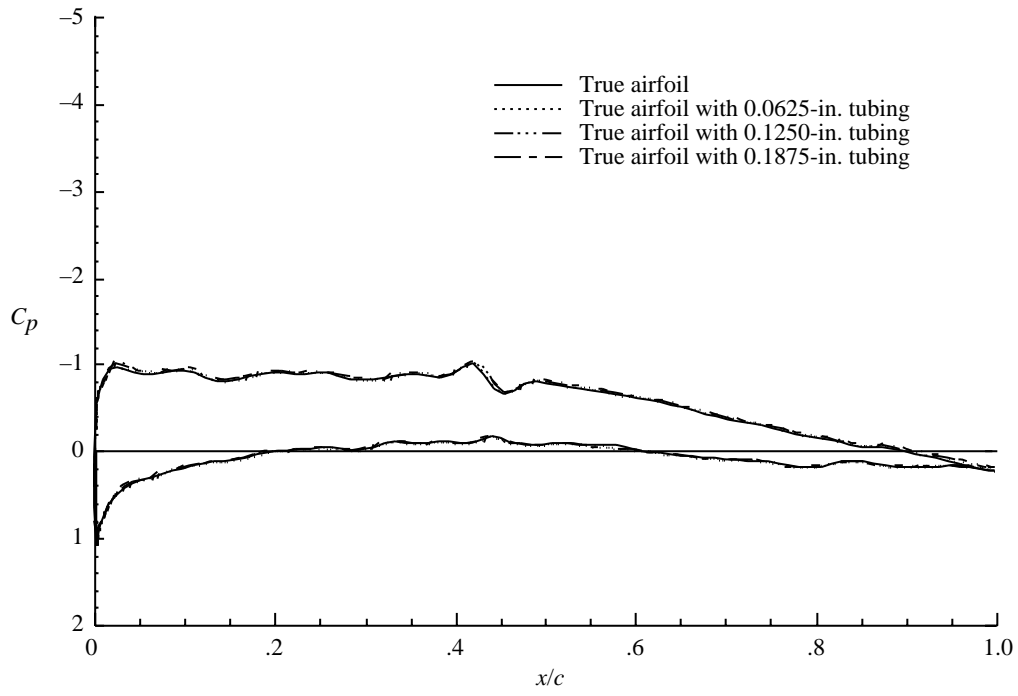


Figure 11. Computed pressure distribution data for $C_L = 0.518$, $\alpha (2D) = 3.3^\circ$, $M_\infty = 0.16$, and $R_c = 4.8 \times 10^6$.

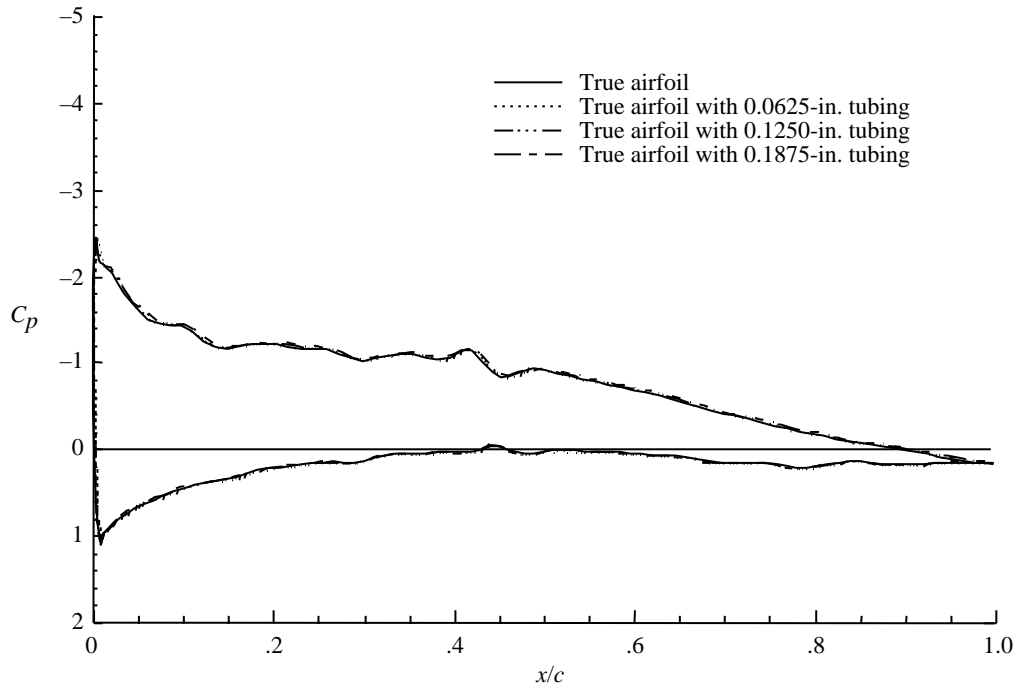


Figure 12. Computed pressure distribution data for $C_L = 0.824$, $\alpha (2D) = 6.6^\circ$, $M_\infty = 0.13$, and $R_c = 3.75 \times 10^6$.

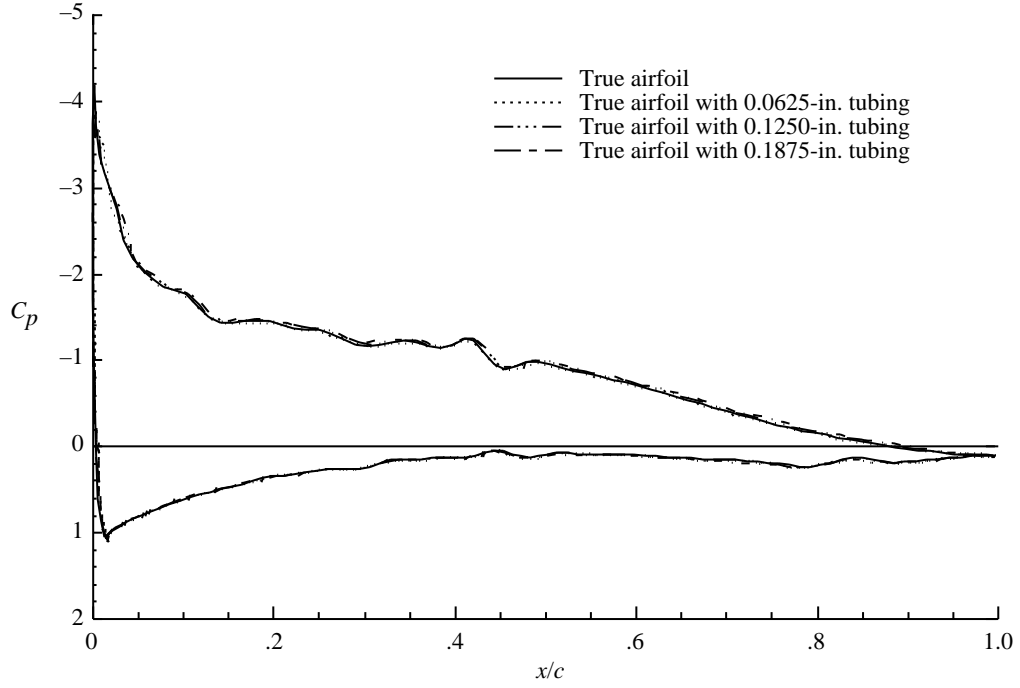


Figure 13. Computed pressure distribution data for $C_L = 1.131$, $\alpha (2D) = 9.0^\circ$, $M_\infty = 0.11$, and $R_c = 3.22 \times 10^6$.

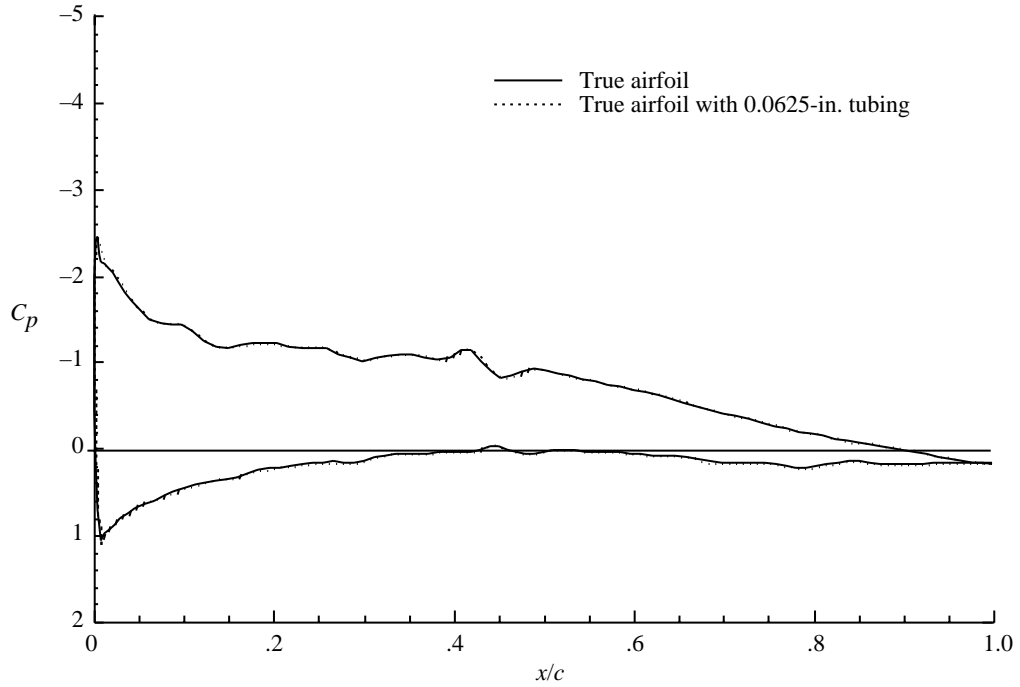


Figure 14. Computed pressure distribution data for OD = 0.0625 in., $C_L = 0.824$, $\alpha (2D) = 6.0^\circ$, $M_\infty = 0.13$, and $R_c = 3.75 \times 10^6$.

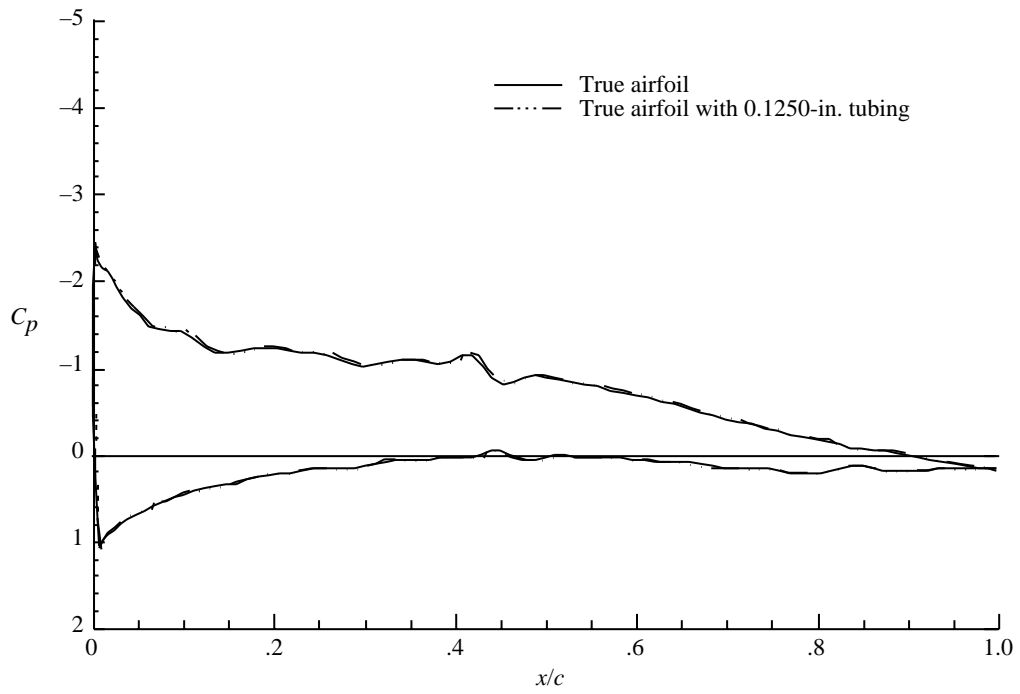


Figure 15. Computed pressure distribution data for OD = 0.1250 in., $C_L = 0.824$, α (2D) = 6.6° , $M_\infty = 0.13$, and $R_c = 3.75 \times 10^6$.

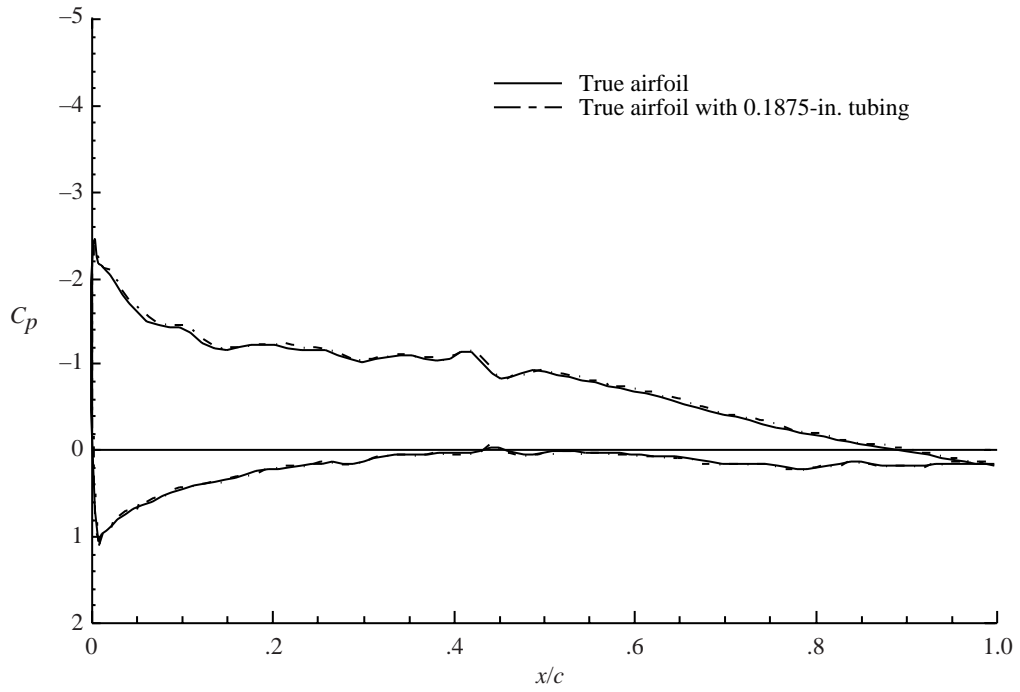


Figure 16. Computed pressure distribution data for OD = 0.1875 in., $C_L = 0.824$, α (2D) = 6.6° , $M_\infty = 0.13$, and $R_c = 3.75 \times 10^6$.

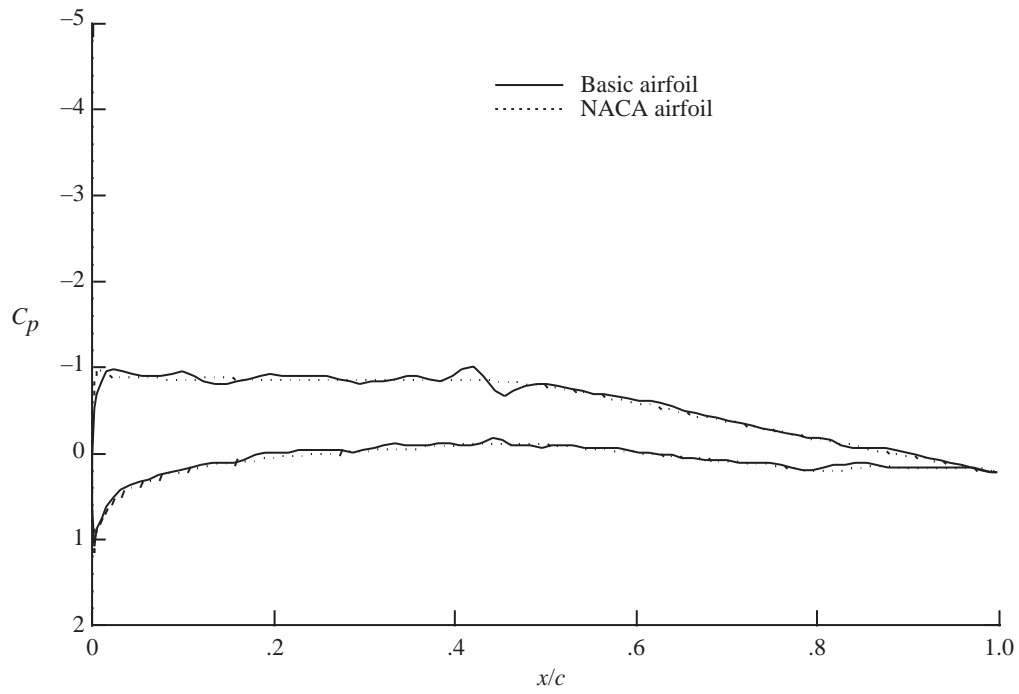


Figure 17. Computed pressure distribution data for $C_L = 0.518$, α (2D) = 3.3° , $M_\infty = 0.16$, and $R_c = 4.8 \times 10^6$.

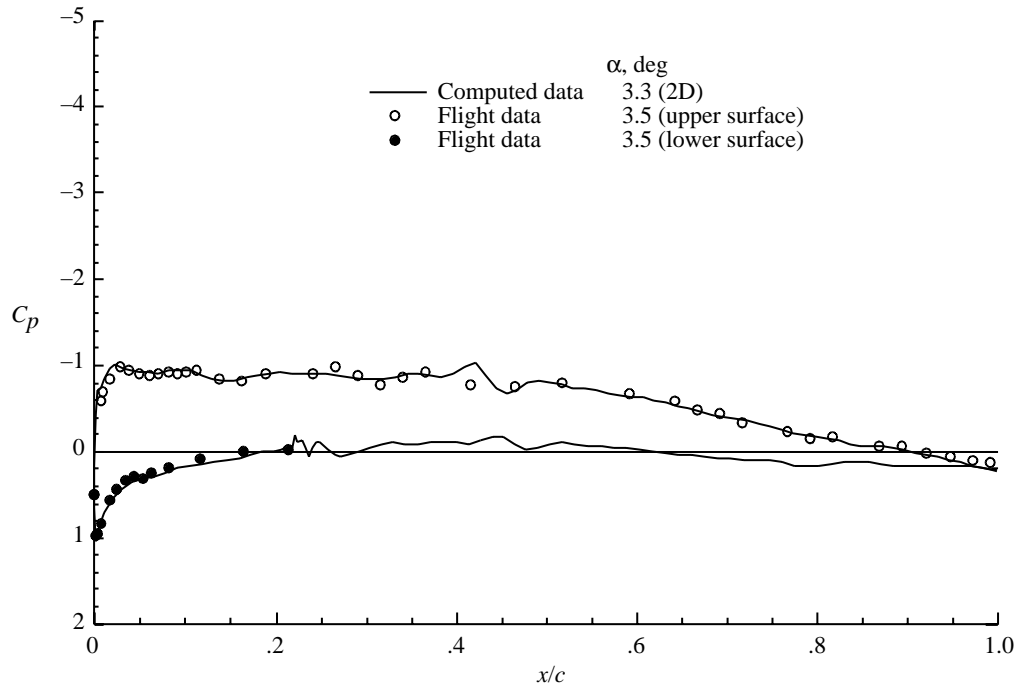


Figure 18. Computed and flight pressure distribution data for OD = 0.0625 in., $C_L = 0.519$, $M_\infty = 0.16$, and $R_c = 4.8 \times 10^6$.

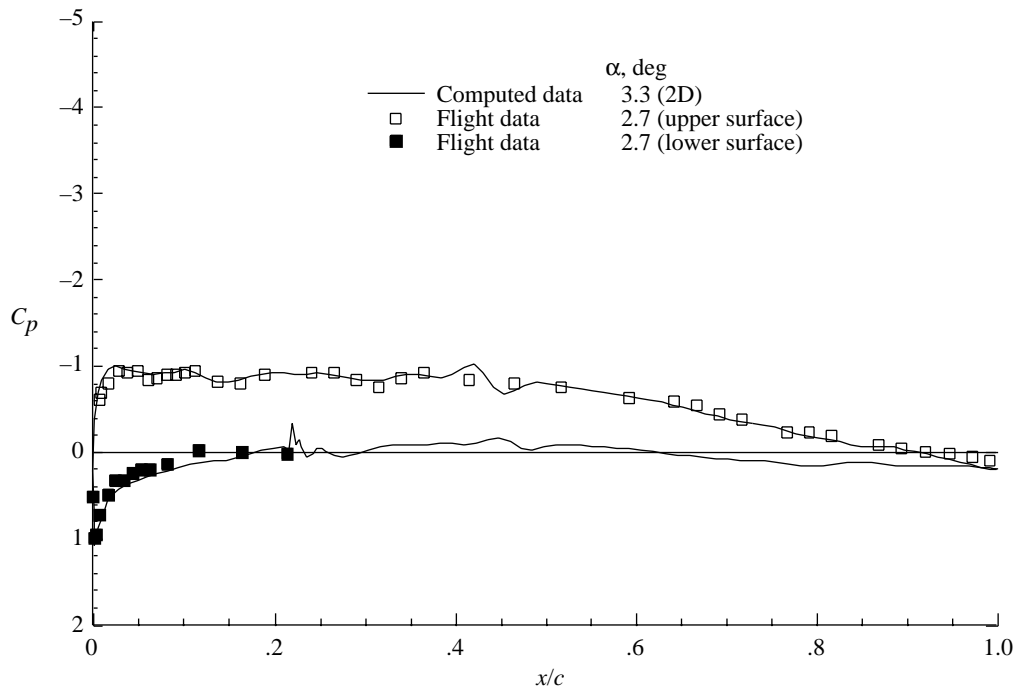


Figure 19. Computed and flight pressure distribution data for OD = 0.1250 in., $C_L = 0.519$, $M_\infty = 0.16$, and $R_c = 4.95 \times 10^6$.

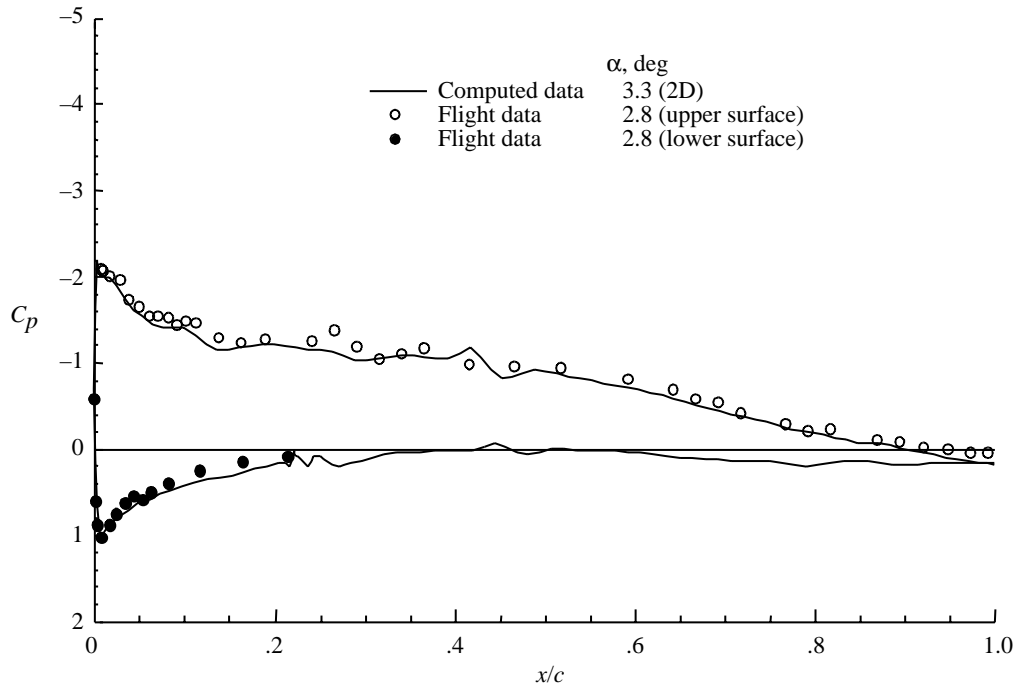


Figure 20. Computed and flight pressure distribution data for OD = 0.1875 in., $C_L = 0.519$, $M_\infty = 0.16$, and $R_c = 4.5 \times 10^6$.

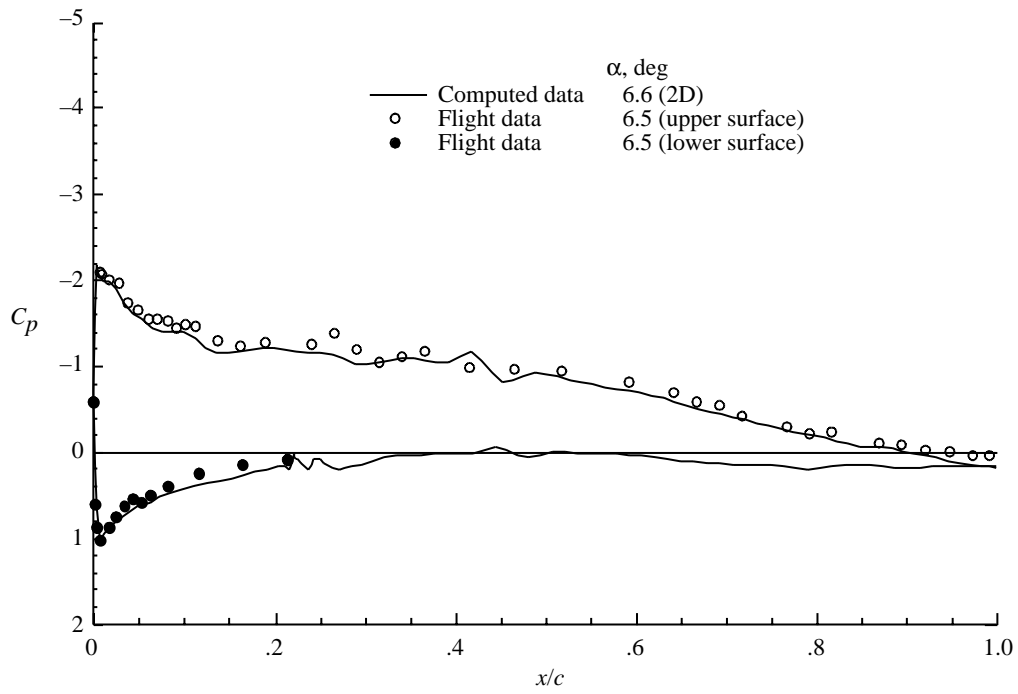


Figure 21. Computed and flight pressure distribution data for OD = 0.0625 in., $C_L = 0.825$, $M_\infty = 0.13$, and $R_c = 3.75 \times 10^6$.

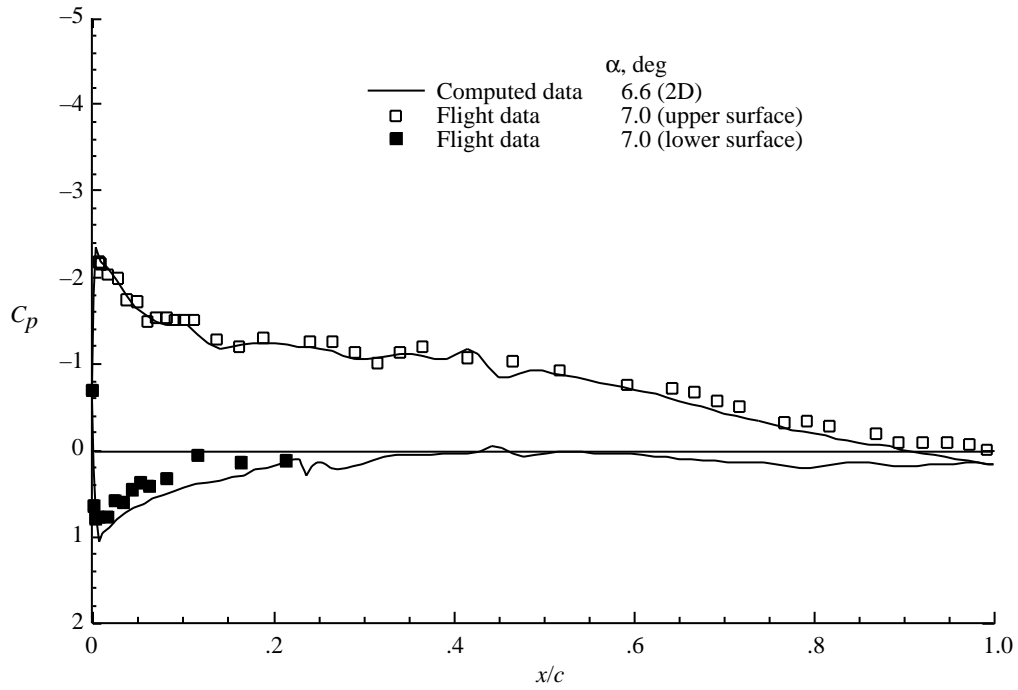


Figure 22. Computed and flight pressure distribution data for OD = 0.1250 in., $C_L = 0.824$, $M_\infty = 0.13$, and $R_c = 3.9 \times 10^6$.

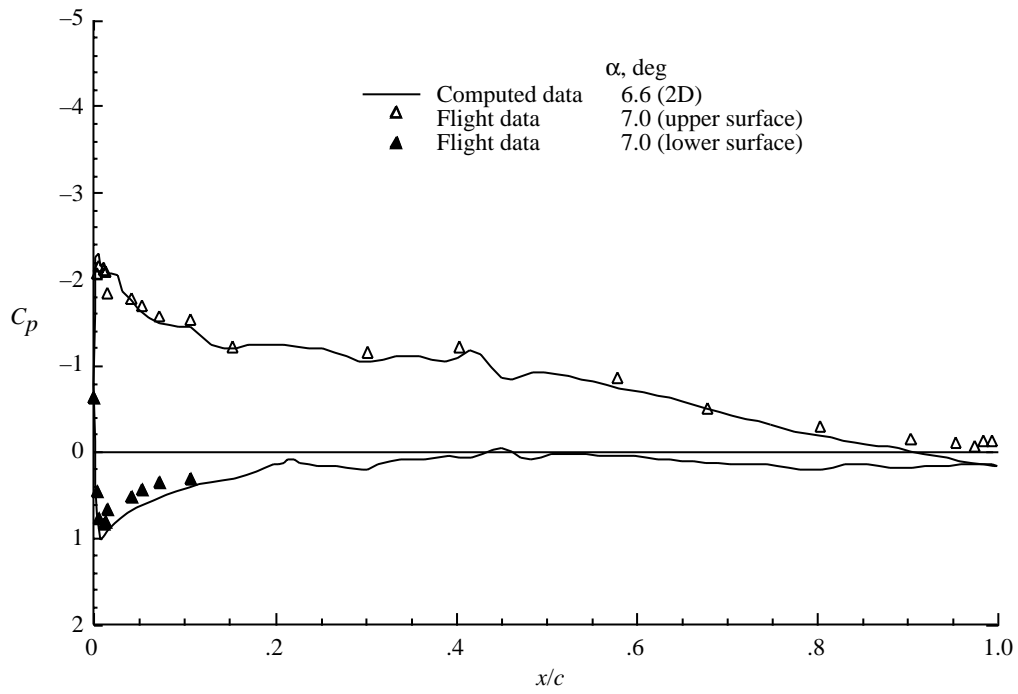


Figure 23. Computed and flight pressure distribution data for OD = 0.1875 in., $C_L = 0.824$, $M_\infty = 0.13$, and $R_c = 3.9 \times 10^6$.

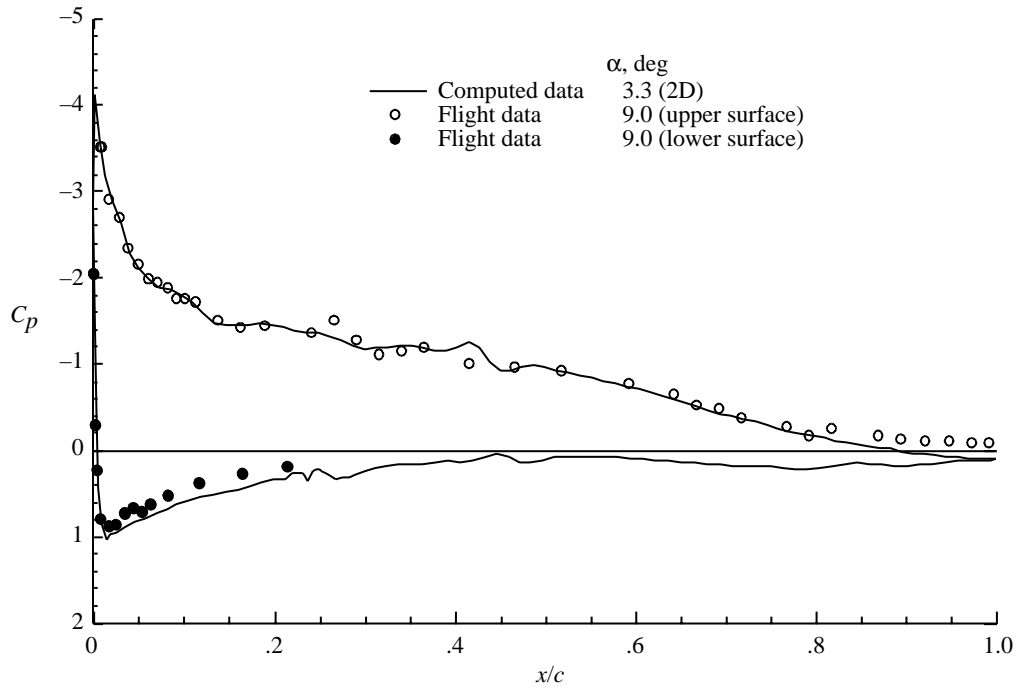


Figure 24. Computed and flight pressure distribution data for OD = 0.0625 in., $C_L = 1.131$, $M_\infty = 0.11$, and $R_c = 3.22 \times 10^6$.

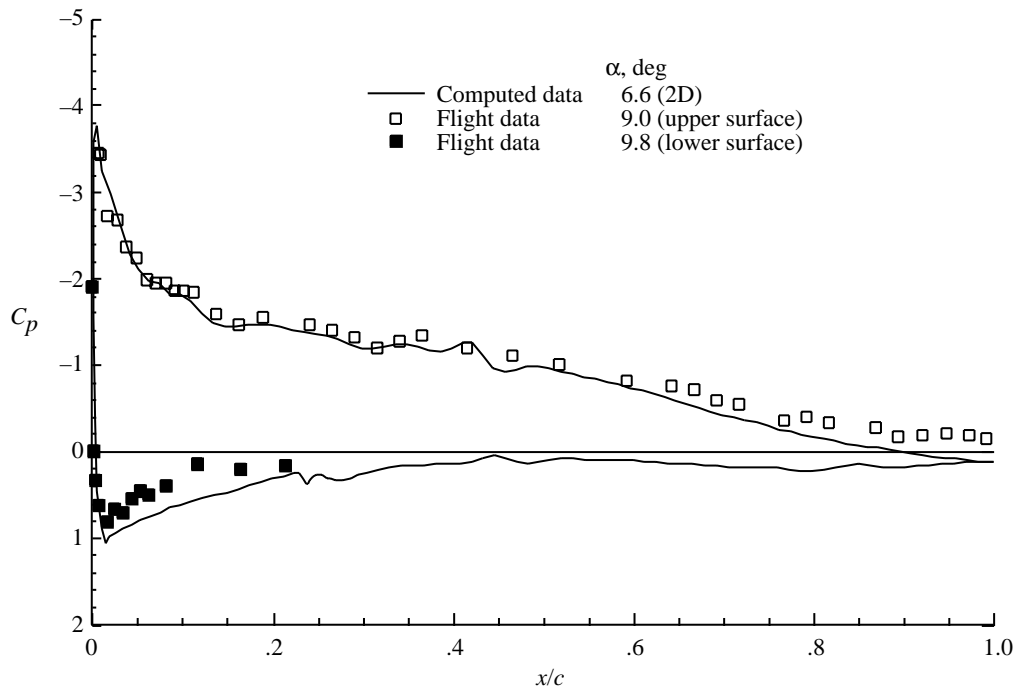


Figure 25. Computed and flight pressure distribution data for OD = 0.1250 in., $C_L = 1.131$, $M_\infty = 0.11$, and $R_c = 3.7 \times 10^6$.

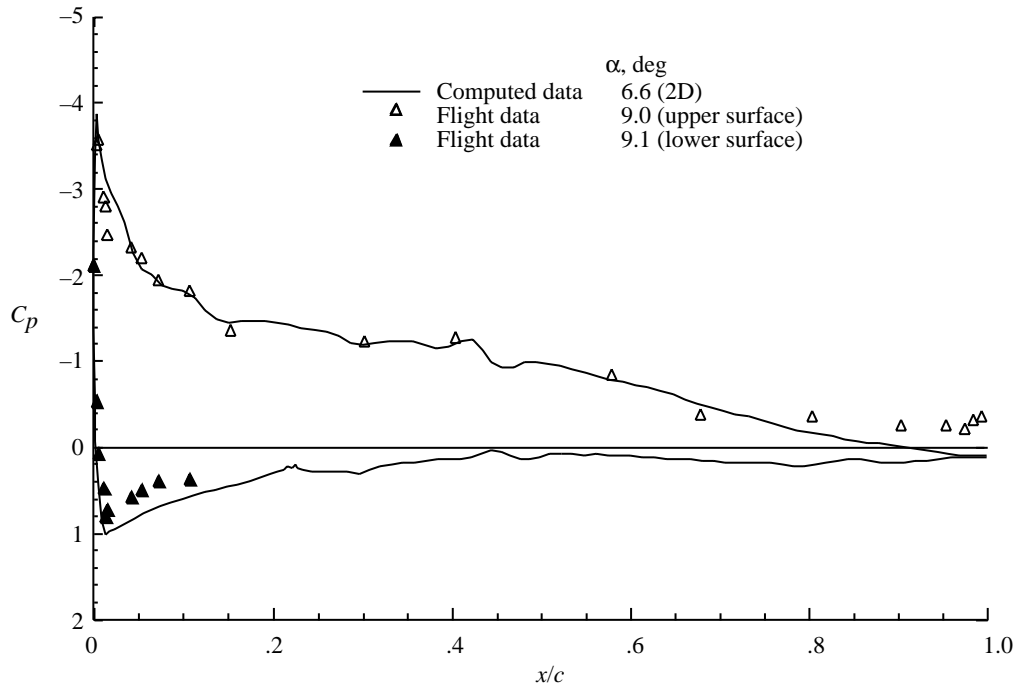


Figure 26. Computed and flight pressure distribution data for OD = 0.1875 in., $C_L = 1.131$, $M_\infty = 0.11$, and $R_c = 3.1 \times 10^6$.

REPORT DOCUMENTATION PAGE			Form Approved OMB No. 0704-0188	
Public reporting burden for this collection of information is estimated to average 1 hour per response, including the time for reviewing instructions, searching existing data sources, gathering and maintaining the data needed, and completing and reviewing the collection of information. Send comments regarding this burden estimate or any other aspect of this collection of information, including suggestions for reducing this burden, to Washington Headquarters Services, Directorate for Information Operations and Reports, 1215 Jefferson Davis Highway, Suite 1204, Arlington, VA 22202-4302, and to the Office of Management and Budget, Paperwork Reduction Project (0704-0188), Washington, DC 20503.				
1. AGENCY USE ONLY (Leave blank)		2. REPORT DATE November 2001		3. REPORT TYPE AND DATES COVERED Technical Memorandum
4. TITLE AND SUBTITLE Flight Investigation of the Effects of Pressure-Belt Tubing Size on Measured Pressure Distributions			5. FUNDING NUMBERS WU 706-62-21-03	
6. AUTHOR(S) Natale A. Rivers, Cornielious P. van Dam, Phillip W. Brown, and Robert A. Rivers				
7. PERFORMING ORGANIZATION NAME(S) AND ADDRESS(ES) NASA Langley Research Center Hampton, VA 23681-2199			8. PERFORMING ORGANIZATION REPORT NUMBER L-18078	
9. SPONSORING/MONITORING AGENCY NAME(S) AND ADDRESS(ES) National Aeronautics and Space Administration Washington, DC 20546-0001			10. SPONSORING/MONITORING AGENCY REPORT NUMBER NASA/TM-2001-209857	
11. SUPPLEMENTARY NOTES Natale A. Rivers, Phillip W. Brown, and Robert A. Rivers: Langley Research Center, Hampton, VA; Cornielious P. van Dam: University of California at Davis, Davis, CA.				
12a. DISTRIBUTION/AVAILABILITY STATEMENT Unclassified-Unlimited Subject Category 05 Availability: NASA CASI (301) 621-0390			12b. DISTRIBUTION CODE	
13. ABSTRACT (Maximum 200 words) The pressure-belt technique is commonly used to measure pressure distributions on lifting and nonlifting surfaces where flush, through-the-surface measurements are not possible. The belts, made from strips of small-bore, flexible plastic tubing, are surface-mounted by a simple, nondestructive method. Additionally, the belts require minimal installation time, thus making them much less costly to install than flush-mounted pressure ports. Although pressure belts have been used in flight research since the early 1950s, only recently have manufacturers begun to produce thinner, more flexible tubing, and thin, strong adhesive tapes that minimize the installation-induced errors on the measurement of surface pressures. The objective of this investigation was to determine the effects of pressure-belt tubing size on the measurement of pressure distributions. For that purpose, two pressure belts were mounted on the right wing of a single-engine, propeller-driven research airplane. The outboard pressure belt served as a base-line for the measurement and the comparison of effects. Each tube had an outer diameter (OD) of 0.0625 in. The inboard belt was used to evaluate three different tube sizes: 0.0625-, 0.1250-, and 0.1875-in. OD. A computational investigation of tube size on pressure distribution also was conducted using the two-dimensional Multielement Streamtube Euler Solver (MSES) code.				
14. SUBJECT TERMS Pressure-belt; Wing surface pressure; Pressure coefficient; Stagnation sensor			15. NUMBER OF PAGES 46	
			16. PRICE CODE	
17. SECURITY CLASSIFICATION OF REPORT Unclassified	18. SECURITY CLASSIFICATION OF THIS PAGE Unclassified	19. SECURITY CLASSIFICATION OF ABSTRACT Unclassified	20. LIMITATION OF ABSTRACT UL	